Experimental analysis
of a self-healing ionomer in a tank
with an internal aluminium filler

Andrea Galbiati
786395

«La preoccupazione dell'uomo e del suo destino devono sempre costituire l'interesse principale di tutti gli sforzi tecnici. Non dimenticatelo mai in mezzo a tutti i vostri diagrammi ed alle vostre equazioni.»

Albert Einstein

Acknowledgments

Abstract

In the last fifteen years, the behaviour of self-healing ionomers after ballistic impact has been explored in different studies, considering different testing conditions and materials. In the present thesis, an experimental campaign was performed in water environment similar to what already done in precedent works for air. A Surlyn®8940 square panel 120 mm wide and with different thicknesses from 1 to 3 mm has been used during the tests. Impacts were performed with spherical steel balls of diameters ranging from 6 to 16.67 mm, accelerated to 180 m/s.

Two configurations were explored. In the first one, a ionomer panel was mounted on one side of a special tank, equipped with pressure transducers in order to track the pressure wave due to the projectile impact. In the latter, an internal aluminium filler (Explosafe®) was placed inside the tank too.

Results showed that the presence of the fluid increased the self-healing capabilities, which were however reduced by the internal aluminium filler. The contribution in terms of sloshing reduction due to Explosafe® was always relevant, while the pressure peak showed some opposite results and it was not possible to conclude that Explosafe® was always effective.

Future applications encompass a wide range of products involving a fluid containment, from tyres or fuel tanks in the automotive field to pressurized systems or liquid tanks in the space field.

Keywords: self-healing, ionomer, Explosafe®, tank, aluminium filler

Sinossi

Il comportamento di ionomeri autoriparanti a seguito di impatto balistico è stato oggetto di diverse ricerche negli ultimi quindici anni. In tali studi, sono state considerate diverse condizioni di prova e anche diverse tipologie di materiali ionomerici. In questo lavoro di tesi, è stata svolta una campagna sperimentale su un unico tipo di ionomero, un prodotto della Dupont il cui nome commerciale è Surlyn® 8940, in una configurazione sperimentale il cui lato di uscita del proiettile era posto in contatto con acqua a temperatura ambiente. Il pannello di ionomero era di forma quadrata e con lato di 120 mm. Il suo spessore, invece, era variabile tra 1 e 3 mm. Gli impatti sono stati svolti con sfere d'acciaio di diametro variabile da 6 a 16.67 mm, alla velocità di 180 m/s.

Il parametro caratteristico usato per studiare il comportamento autoriparante è rappresentato dal rapporto dei due parametri variabili: spessore del pannello e diametro del proiettile.

Il serbatoio sperimentale era di circa 3 litri di capienza e di forma cilindrica. Su un lato di base del cilindro veniva posto il pannello di ionomero. Lungo il serbatoio sono stati inseriti dei sensori di pressione, al fine di misurare l'onda che si sviluppava all'interno a seguito dell'impatto.

La riparazione in caso di acqua è stata pressoché istantanea e solamente alcuni getti di piccole dimensioni sono fuoriuscite dal foro di ingresso del proiettile nei primi millisecondi.

Oltre alla configurazione classica con acqua nel serbatoio, è stato studiato il comportamento autoriparante nel caso in cui anche un riempitivo metallico, il cui nome commerciale è Explosafe®, era stato posto all'interno del serbatoio.

I risultati hanno mostrato come, nel caso senza Explosafe, la riparazione si sia dimostrata più efficace rispetto alle condizioni di ionomero in aria. Tuttavia, nel caso con il riempitivo interno, le capacità di riparazione sono diminuite a livelli anche inferiori a quelli verificati in aria. Per quanto riguarda il fenomeno di sloshing, invece, Explosafe si è dimostrato molto efficace, ma i risultati sono stati contrastanti per quanto riguarda l'effettiva capacità di ridurre il valore di picco dell'onda di pressione negli istanti immediatamente successivi all'impatto.

Possibili applicazioni pratiche di questi materiali riguardano principalmente sistemi adibiti al contenimento di fluidi, come per esempio serbatoi o pneumatici nel campo automobilistico, o sistemi di pressurizzazione di ambiente o serbatoi in ambito aeronautico e spaziale.

Index

Index of Figures

Index of Tables

1. INTRODUCTION

1.1   Self-healing materials

1.1.1   Damage and biomimetic behaviour

In every engineering application, damage is an element that cannot be neglected. Nowadays the main strategies to improve the reliability of materials are based on the so called *damage management* philosophy: a strict program of maintenance and inspections is implemented and executed for every sophisticated machine.

However, that cost has a high impact on the operating cost of the machine itself, and, obviously, not all kind of damages can be safely managed.

If we think about nature, we have an everyday life experience with the *healing* capabilities of tissues. A mechanism so simple for nature is yet so difficult to implement in human mechanical applications.

Recent studies have shown promising developments for a new class of materials, called *self-healing*, that have the ability to restore their mechanical features quite completely even after damage.

Therefore, drawbacks of classical materials are overcome by self-healing materials, which are an example of *damage prevention* philosophy.

Though the field of self-healing materials presents high promises, it is still difficult to understand clearly the healing process and the crack kinetics of these kind of materials. This frontier of knowledge is one of the next steps to be undertaken by research programs.

An additional challenge is also the autonomic detection of cracks and its subsequent healing: materials shall be able to detect a crack and to start the healing process autonomously. If external intervention is needed, the problem of detection persists, and maintenance still has a paramount importance.

1.1.2   Healing

Self-healing is the ability of a material to repair damages automatically and autonomously [1]. This process can develop with or without an external intervention, from which the materials can be divided in two classes:

o *autonomic*, where healing takes place without any intervention;

o *non-autonomic*, where there is the need of human intervention in the sense of an external trigger intervention.

Self-healing in a material occurs by release of healing agent or by reversible crosslink in its molecular structure.

The former reparation technique is possible through:

o microcapsules embedment;

o hollow fibre embedment;

o microvascular systems.

The class of reversible cross-link materials encompasses:

o Diels-Alder (DA) and Retro-DA Reactions;

o ionomers;

o supramolecular polymers.

1.1.2.1 Self-healing strategies

Microcapsule. The first mechanism bases its functioning on occurring an appropriate chemical reaction, which leads to a polymerization process.

Microcapsules are put inside a composite material containing a particular resin since the beginning; resin is the "repairing agent". When a fracture occurs inside the material, capsules located in that area break, thus releasing the resin. This resin flows inside the polymeric matrix, where it polymerize thanks to the presence of the catalyst. As a result, the crack is filled and the original mechanical properties of the material are restored.

Although the microcapsules' invention is one of the most innovative development within self-healing materials, they are not always the right solution for all the fracture and damaging cases.

Damages of big proportion, as those caused by a projectile impact, cannot be repaired by using microcapsules. Moreover, this type of solution does not allow a second use, because microcapsules, once broken, are not able to work again.
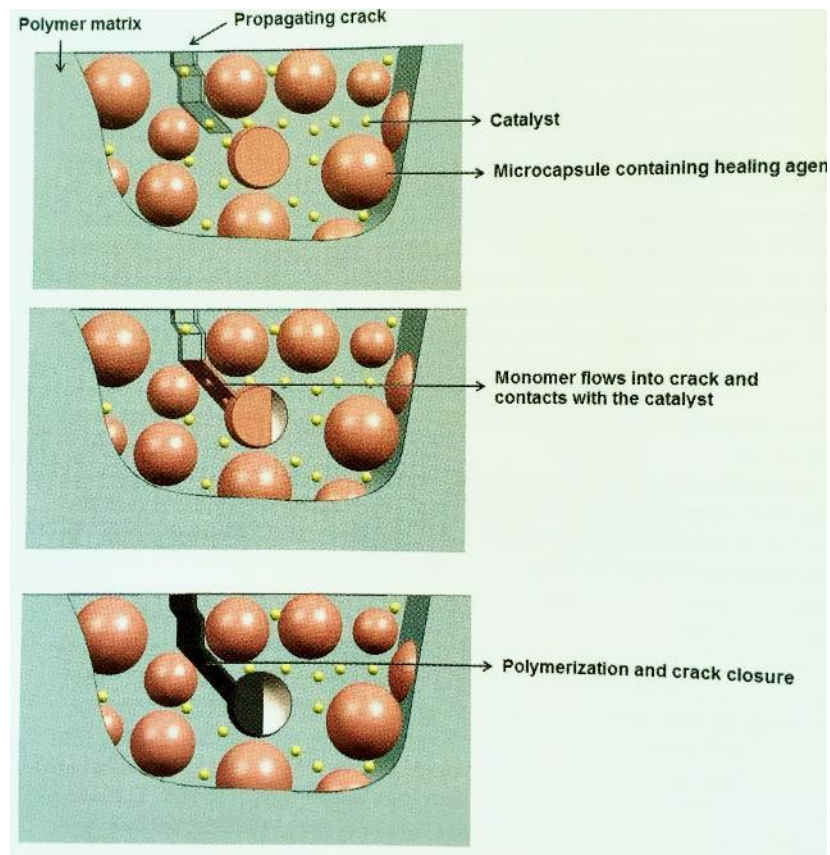
Figure 1 - Self-healing concept using embedded microcapsules [1]

Fibres containing resin. The second type of self-healing materials involves materials reinforced by fibres containing resin. Fibres are generally made of glass or carbon fibres. This kind of configuration can be an advantage in terms of structural behaviour, since long fibres can increase the resistance features of a material.

In a similar way to what described for microcapsules, when a damage occurs (i.e. a fracture or a delamination) the broken fibres release the resin and the catalyst: they react one another and fill the crack. Also in this case the functioning is based on a chemical reaction, which is spontaneous or activated by temperature or UV radiation.
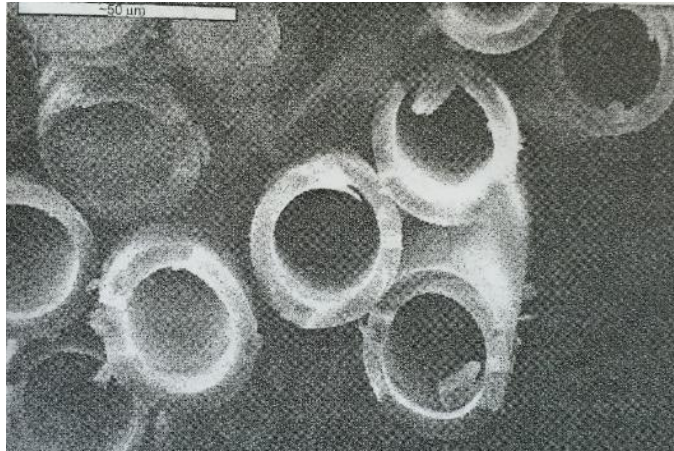
Figure 2 – Optical micrographs of hollow glass fibres [1]
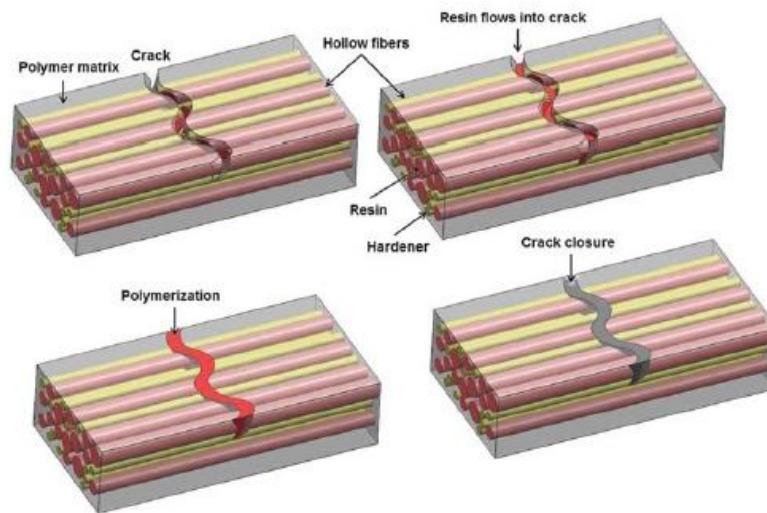
Figure 3 – Hollow fibres healing schematic concept [1]

Repairing through heating. The last mechanism belongs to the group of materials requiring an external assistance in order to start the repairing. External intervention is in this case the heating. It has been observed that some polymers (i.e. polystyrene and polyethylene) seal one another if they are put together beyond their temperature of glass transition phase [1].

However, in order to obtain a repairing, the two faces of a crack, made in a polystyrene sample, have to be kept close (e.g. with the aid of a vice), and the temperature has to

be risen. In this way the material, warming up, expands, the two surfaces are brought together and they weld again.

A huge disadvantage of this technique is the long time required (from few minutes to few hours) and the presence of a continuous and controlled external force that has to be applied in order to keep the broken parts well bonded.

Diels-Alder (DA) and Retro-DA Reactions. Among the examples of reversible healing polymers, the Diels-Alder (DA) reaction and its retro-Diels-Alder (RDA) analogue seems to be very promising due to its thermal reversibility. In general, the monomers containing the functional groups such as furan or maleimide form two carbon-carbon bonds and construct the polymer through DA reaction. This polymer, if heated, breaks down to its original monomeric units via RDA reaction and then reforms the polymer upon cooling.
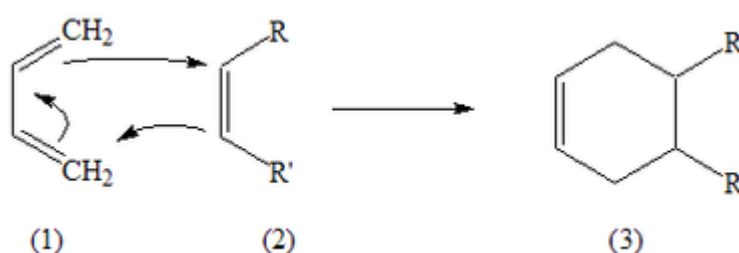
Figure 4 – A generic DA reaction scheme

Supramolecular. The concept of supramolecular materials relies on the use of non-covalent, transient bonds. Natural reversibility of supramolecular interactions, for example given by hydrogen bonding, leads to materials with a lack of mechanical strength. Undamaged material is made up of polymer chains which form a network of reversible sticker-like bonds. Thus, the strength of the material is generated by the stickiness of the supramolecular bonds. When mechanical stress is applied to the material, it will be the weaker supramolecular bond which fails. The generated new interface contains a multitude of now unbounded *sticky* supramolecular bonds. The closure of the gap by means of reformation of supramolecular bonds occurs after a recombination of the two fragments. Assembly forces such as metal-ligand, interactions and hydrogen bonding are used to design supramolecular polymers [2].
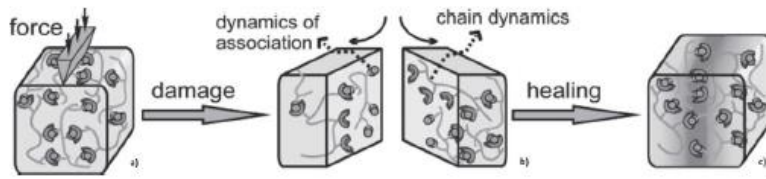
Figure 5 – Self-healing mechanism for a supramolecular material [3]

Probably, the most known supramolecular material is Reverlink®, a rubber which has been designed and developed by Arkema and Professor Ludwik Leibler's team at the Ecole Superieure de Physique et de Chimie Industrielle.

With its tensile module of 90 MPa, Reverlink® is one of the most performant supramolecular rubbers.

Figure 6 – Arkema Reverlink HR

Ionomers are a class of polymers, with 20% of ions content. These ions create aggregates, which play an important role in defining their physical and mechanical properties. In the last forty years, several studies have been carried out about the relation between these polymers' structure and their properties. Also some commercial applications use them, mostly in food and cosmetics packaging or in sport items (e.g. golf balls). However, researches as ionomers with self-healing capabilities have been carried out since no longer than ten years.

The self-healing phenomenon for this type of ionomers shows up spontaneously with no external intervention. Reparation is caused by the energy due to impacts: a part of the kinetic energy of the projectile is transferred to the material in the form of heat and elastic energy. If the ballistic impact brings enough energy to the ionomer, the material is locally melted, and the fused part experiences an elastic return in its original position. The following solidification of the material completes the healing. All these phases take place in some centesimal of millisecond only.
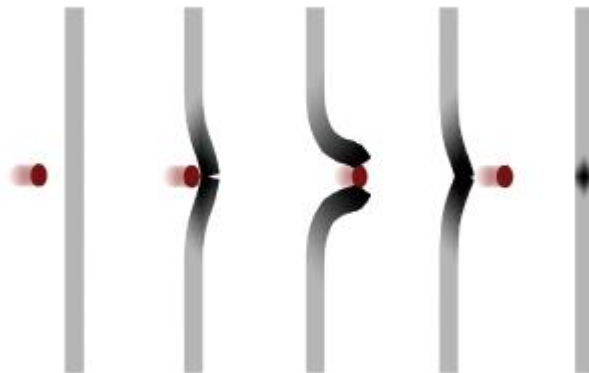
Figure 7 – Schematic sequence of healing during ballistic impact

Ionomers are realized by a copolymer neutralization process. They come from copolymers containing repetition of ionic and non-ionic groups. The ionic content is different from one ionomer to another, according to the number of neutralized acid groups.

Over the past few years different models have been proposed with the aim to explain the specific molecular structure of these materials [8]. In 1970 Eisenberg suggested a theoretical model, which described the tendency of ionic pairs to gather around the region containing exclusively ionic material. These aggregates, which are entirely ionic and composed by a very low mass and a strong electrostatic interaction, are called *multiplets*. The shape and the number of ionic pairs in every single multiplet depend on different factors, such as the flexibility of the polymeric chain, its dielectric constant and the ionic content. For example, a low dielectric constant and a low glass transition temperature (T_g) of the guest polymer facilitate ionic pairs aggregation; on the contrary, high dielectric constants and high T_g inhibit the creation of multiplets.

Moreover, electrostatic forces play a very important role: pairs of little and highly polar ions interact more strongly, creating bigger and steady groups.

Due to the multiplets presence, there is a lower flexibility within the polymeric chain. The level of flexibility reduction depends on several factors, such as the bond between the chain and multiplet, the molecular weight, the density and the chain expansion near the multiplet.

The Eisenberg's model about ionomers explains also how the different multiplets form into clusters. A single multiplet, including its region of reduced flexibility, extends for no longer than 25/30 Å. Increasing the number of ions, multiplets are neared one to

another and, due to the electrostatic interaction between them, an area of reduced flexibility is originated within the polymeric chain, which is named *cluster*.
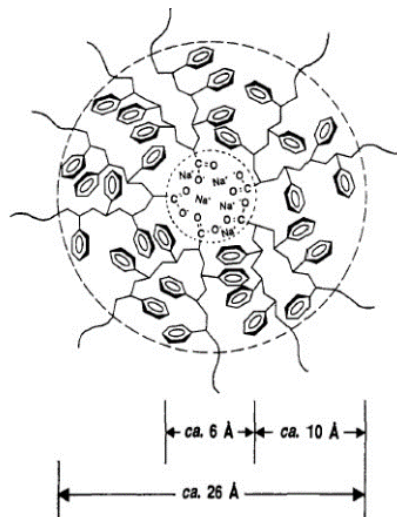
Figure 8 – Mobility-reduced region around a multiplet

The different shapes of multiplets and ionic aggregates are responsible for the physical and mechanical properties of these materials. Bonds within ionomers are thermo-reversible and this is the reason why they are self-healing materials. At room temperature the ionomer structure is very orderly and can be distinguished in three different regions: crystals, the amorphous structure and clusters.

Increasing the temperature causes a state of disorder within clusters (for most of ionomers it happens at around 50 °C), which produces relaxing among bonds and flexibility growing. Crystals vanish when the temperature reaches the fusion point (around 90 °C). Crystals form again reversing the process, i.e. turning down the temperature, but the ordered reorganization of clusters requires more time.

Another meaningful aspect regarding the ionomers' morphological structure is the ion hopping phenomenon, namely the tendency of an ion to "jump" from an aggregate into another. Ions aggregates can be found in the melted polymer also at high temperatures (till approximately 300 °C), even though they are in a disordered configuration; their presence allows much more viscosity to these materials compared to the one founded in similar, but non ionic, polymers.
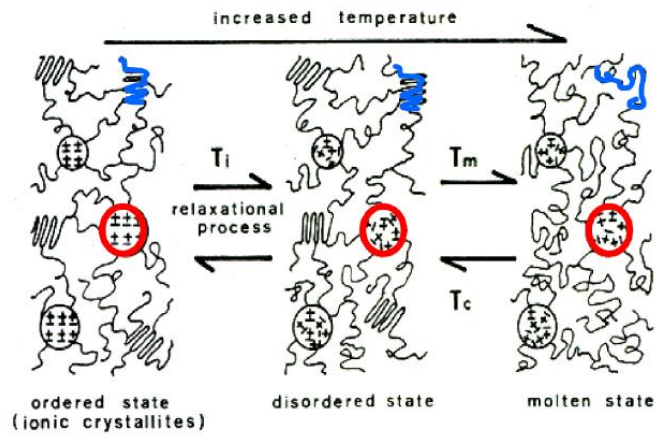
Figure 9 – Ionomer morphological structure, with ionic aggregates (in red) and thicker primary cells (in blue) in evidence

Ionic aggregates are dynamic and there is, also, an average time which indicates how long an ionic group stays in a specific aggregate before jumping into another one. Thanks to this feature, relaxation of the polymeric chain is enabled. Thus, the polymer can melt without requiring that also the other ionic aggregates melt with it. This performance let the material be elastic also when it is melted, which is an extremely relevant factor involved in the self-healing process.
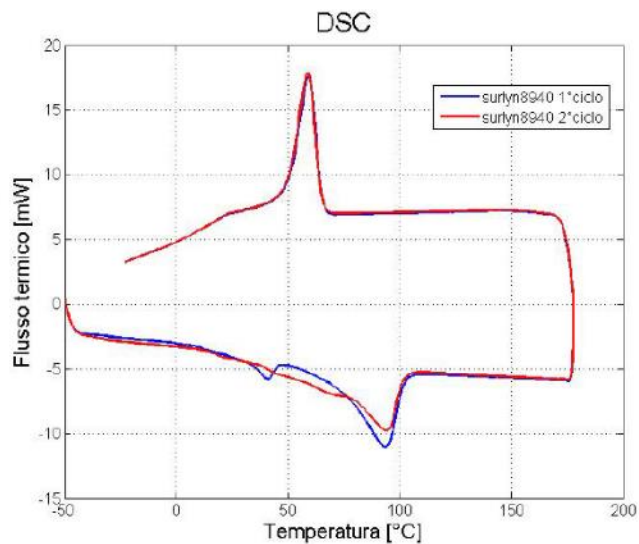
Figure 10 – DSC test for Surlyn8940 [4]

1.1.3 Applications

The real change that self-healing materials can bring to the material industry is based on their ability to heal autonomously.

However, some challenges remain to be solved in order to commercially expand their field of applicability. Among them, a core role is played by the autonomic detection of cracks and its subsequent healing: materials shall be able to detect a crack and to start the healing process by themselves. If external intervention is needed, the problem could be detection. Another problem is related with their mechanical properties, which are quite low as any kind of polymer. In the field of mechanical industry, instead, a lot of applications would benefit from self-healing material if their stiffness would be higher. To this extent, sandwich structure can be a strategy to mitigate this drawback.

In general, the field of possible self-healing materials application is huge: metals, polymers, ceramics, concretes, coatings. In every field, studies are constantly published and a lot of progress is being made, since healing feature is a benefit both for economical and safety purposes.

However, today, only a few self-healing materials have experienced a further development than a laboratory implementation level.

The very few applications known up to date in the industry are a Nissan pilot coating for cars, some concretes with self-healing capabilities driven by bacteria, a short asphalt segment in the Netherlands [1]. Different studies on self-healing corrosion resistant coatings have been started for different applications, from nuclear plants or turbine machinery. In the medical segment, biocompatible composites can extend the service life of artificial bone, teeth, and so on.

Among self-healing materials, the class of ionomer is the one that is able to recover from one of the most energetic damages: the ballistic impact.

At first instance, the ballistic impact healing field of interest seems to be restricted to military use only. However, also civil and research segments suffer from the ballistic impacts risk, that it is not necessarily related to weapons, but also to any kind of debris with a high velocity.

In the aerospace sector, driven always by severe requirements in terms of weight and reliability, some examples are tanks (both for fuel or water), pressurized systems such as tyres or spacecraft inhabited modules [5] [6]. Always in the space segment, interests could be also for classical MMOD (i.e. Micro Meteoroids Orbital Debris protection [7] [8] [9] [10]) risk management.

The risk of debris damage for space applications does not concerns only the orbital phases, but also the launch phase. This is in fact a very critical phase of the mission, as the number of failures (or causes of failures, as in the case of the Space Shuttle Columbia) can witness. Columbia's case is paradigmatic: the loss of the shuttle was caused by the thermal fault of part of the cover tiles, due to the ejection of fragments from the main rocket during the first phases of launch. A recovery capability to such a critical element could highly extend the reliability of the whole system.

Always in the space industry, inflatable and deployable flexible-walled structures have been used in numerous space missions since the dawn of space exploration, as in the case of communications satellites (ECHO, Explorer), missile decoys, space suits, airlocks (Voskhod 2) and impact attenuation airbags (Luna, Pathfinder, MER). The benefits of structures with foldable walls results in advantages in terms of stowage volume and mass reduction. Such materials, on the other hand, suffer the explosion to debris damage, and a self-healing capability to preserve the pressurization could be a key element.

The concept of self-healing could be extended to the walls of classical spacecraft, which are actually sized taking into account the MMOD risk mitigation. However, even using the Whipple layer concept, the first panel hit by a debris (i.e. the external) is subjected to a definitive perforation. Ionomers layers both in the external or internal layers could be an advantage in terms of structural integrity [11].

In the aeronautics field, instead, military aircrafts or helicopters, employed in war zones, can suffer the enemy fire. Historically, the Vietnam war and Iraqi wars, in which flying aircrafts were downed by small arms and automatic fire, demonstrated the importance of preserving the integrity of fuel tanks. More recently, in the Desert Storm war, some 75% of all aircraft losses were related with fuel system. Causes were primarily: fire, explosion, HRAM [12].

However, also in civil aviation, the Concorde accident (Paris, 2000) showed the potential catastrophic effect of debris accelerated to about 200 m/s. In that case, a tyre blow up after the impact with a titanium debris left by the previous airplane during take-off. The exploded tyre hit the wing tank and the fuel started to leak due to perforation. The vicinity with the right engines fed the development of a big fire under the wing, thus creating an aerodynamic surge that did no more permit the manoeuvrability of the airplane. It is even true that modern commercial airplane are not designed in the same way as the Concorde was, but in future aircraft architecture the same strategies could be applied and such a criticality shall be solved.

1.2   Explosion prevention system: internal aluminium filler

When a projectile hits a fuel tank, the response of the container wall, the liquid and the vapour contents determines whether the projectile will penetrate or just bounce off. Ideally, we would like the projectile to bounce off and not penetrate the wall. The projectile velocity limit for this situation is called ballistic limit. If the wall is breached, then the fuel can spill and cause a fire. In some cases, the dynamics of the projectile impact can cause the container to pressurize and an explosion can be generated.

The explosion event has been a major cause of military aircraft loss in combat, and in particular way for helicopters, which are more exposed to risk because of lower flight altitude and velocity. Over the years, many techniques aiming to prevent or suppress such explosions have been explored: nitrogen dilution, chemical quenching and polyurethane foam explosion suppression materials have emerged as the primary candidate systems. The field of application of this kind of techniques is not only in the military field, even if it remains the principal beneficiary of these products, but also in other civil applications.

Explosafe is only one of these solutions. It is an expanded metal mesh manufactured from thin aluminium foil. Coiled, or otherwise layered into a three dimensional structure of controlled density, it can be shaped to match the interior geometry of fuel tanks and installed through existing access areas.

The system has the passive, logistics-free advantages of the foam filler materials because of its metallic nature, it is free of limitations on operating temperature (melting point of aluminium is around 600 °C), it is hydrolytically stable, and does not encourage electrostatic charge generation during fuel filling operations, which is the primary disadvantage of polyurethane foam materials.

Explosafe explosion suppression system has been developed in the 1970s by the Explosafe Division of Vulcan Industrial Packaging Limited (VIPL) of Canada, and since its beginnings it was employed in a variety of surface vehicles. Its applications spread into the aerospace and naval field during the following years. Combat aircrafts and helicopters, military automotive and war trucks, patrol boats are some of the military applications where Explosafe has been used, while helidecks and racing motorbikes are two civil applications.

Air Force Wright Air Laboratory (AFWAL) conducted a complete study on Explosafe, in which results of a four-year performance study and qualification test program were presented [13].

Explosafe demonstrated positive capabilities in the fields of ballistic impact, slosh, vibration, compaction, contamination, corrosion, static attenuation, fuel displacement, fuel retention and it was of easy handling. However, installation and removal can present some difficulties. Some problems have been found because of its negative effect on fuel pumps (obstruction, extra differential pressure needed to create the desired flow) and, after 1980s tests, new countermeasures have been carried out by the manufacturer: bigger pellet dimensions or a bag made of Explosafe itself containing a bunch of pellets.

As mentioned before, Explosafe is not the only fire suppression system made from expanded aluminium foil. Competitors are Deto-Stop, Ex-Co, Explo Control, No-Ex, EM2 and others.

However, Explosafe was the first to appear in the late 1970s, and has a solid background of engineering studies and publications for aircrafts applications [14].

1.2.1 Studies on Explosafe

In addition to the AFWAL report, that encompasses different specific reports in a single work, an important research that can help to introduce the present thesis work is the one published by Copland [15].

Copland conducted some tests in order to study how the Explosafe matrix affected the hydrodynamic ram effect. This effect takes place when a high-speed projectile hits and penetrates a liquid filled container. It involves three phases: a shock upon entry, drag from passage through liquid and cavity generation.

In the tests, bullets and spheres of different calibre were fired into 20 and 220 litres fuel containers holding water and diesel fuel. Some of the cans were equipped with Explosafe. Projectiles were traveling at around 870 m/s (Mach 2.6 in air). The presence of the aluminium matrix made things worse in the 20 litres containers. Apparently, the tumbling projectile grabbed hold of the Explosafe and carried it along. This produced a piston effect that did more damage on the exit surface. Spherical rounds did not show this same trend. For the 220 litres drums, the presence of the Explosafe did not appear to make things worse or better.

In Copland report emerged that spheres made less damage in Explosafe material. The proposed explanation is the fact that non-spherical projectiles do tumble during the passage into the liquid, entangling with the filler and thus augmenting their mass, and their destructive effect.

1.3   Main goals of the present thesis and research strategy

In the last years, the behaviour of self-healing ionomers has been studied in different thesis. One of the first complete contribution are the thesis of R. Fall [16] and S. Kalista [17] in 2001. All the works developed inside the Politecnico di Milano research programs were aimed to verify the reparation phenomenon in different conditions and for different materials.

Tests have been done with Surlyn 8940, 8920 and Nucrel, including the variation of parameters such as the impact angle, target thickness, projectile shape, dimensions and speed. Multilayer panels have been tested, in which different materials such as rubbers, honeycomb sandwiches, carbon fibre panels and aramid fabrics were coupled with the ionomer essentially in order to enhance its mechanical characteristics.

Tests were carried at three different sets of speeds: low speed (around 180 m/s), medium velocity (350 - 600 m/s) and hypervelocity (1.2 - 2 km/s).

The present work had two primary goals. The former was to conduct an experimental campaign in water environment similar to what already done in last years in air, in order to have the possibility to compare the results. The second main goal was to test the reparation behaviour of ionomer when an internal aluminium filler, called Explosafe®, was added inside the tank.

Explosafe was already part of a work developed at Politecnico di Milano [18], in which its capabilities in sloshing reduction were verified in case of a 20-litres tank crash at around 5 m/s.

In the present thesis, however, the intention was to compare the pressure waves generated inside the tank in the case with and without Explosafe during a spherical steel impact at around 180 m/s. The only reference to a similar work is the one conducted by Copland [15].

In order to reduce the tested variable to a reasonable amount of work, Surlyn 8940® was selected for the ionomer panel. The choice was driven by the results of previous thesis works, in which it emerged to have the best reparation performance for the whole spectrum of bullet's velocities.

Also bullet shape was fixed to spherical balls, as done in all other theses at Politecnico di Milano, even if in previous works emerged the negative effect of blunt end bodies for both ionomer reparation and Explosafe efficiency.

2. EXPERIMENTAL: methods and test setup

2.1 Material and specimen production

2.1.1 Surlyn® 8940

2.1.1.1 Features

Surlyn is an ionomer by Dupont® [19], whose technical name is *copolymer polyethylene-co-metacylic acid*, with 5.4% mol methacrylic acid, which has been neutralized with a cation. The elementary chemical chain is represented in Figure 11, while its properties are reported in Table 1.
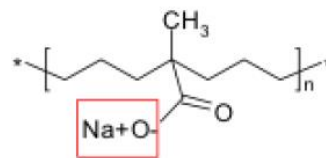
Figure 11 – Surlyn 8940 basic chain

Density	0.95 g/cm³
Melt flow rate (190°C/2.16kg)	2.8 g/ 10 min
Melting point	94 °C
Freezing point	59 °C
Vicat softening point	63 °C

Table 1 – Surlyn 8940 physical and thermal properties

2.1.1.2 Specimen production

Ionomer pellets were dried in vacuum (about 0.1 bar) at 60°C for 5 hours, with the aim to extract humidity from the material.

Square plates (120 × 120 mm) of different thickness (ranging from 1 to 3 mm) were produced by compression moulding at 180°C. Unfortunately, no different specimen sizes were possible because of the machine limitations.

Figure 12 – Ionomer's vacuum drying

Thickness was instead a controllable variable, since it was given by the quantity of material positioned inside the plate of the machine. Reference values are given in the following table.

Thickness [mm]	Surlyn weight [g]
3	52
2	35
1.5	28
1	20

Table 2 - Surlyn 8940 used in order to produce panels with desired thickness

Pressure imposed to the fused polymer inside the compression moulding machine was gradually increased to about 5 kilos on 4" DIA RAM (equivalent to about 5 MPa). The pressure was kept constant for about 3 minutes at the temperature value of 180 °C, which was measured through 2 thermocouples placed inside the upper and lower plates.

In order to avoid contamination and bonding to the machine's plates, a thin Teflon panel was interposed between Surlyn and the walls.

Before testing, specimens were stored in an environmental chamber at 23°C and 50% RH for 1 month in order to reach stable mechanical properties.

Figure 13 – Surlyn® 8940 compression moulding

A total number of 57 panels have been produced for the present thesis work, divided in the following scheme:

- 9 of 1 mm thickness;
- 11 of 1.5 mm;
- 20 of 2 mm;
- 14 of 3 mm;
- 2 of 3.5 mm;
- 1 of 4 mm thickness.

Figure 14 – final ionomer panel

2.1.2 Explosafe®

Explosafe is made of an aluminium sheet (around 0.05 mm), manufactured by slitting and expanding the foil through two mechanical machines in order to create hexagonal holes [13]. The average density of Explosafe® is 30 kg/m^3, even if it is dependent on the aluminium foil thickness. Then, the aluminium cells can be grouped in various ways with the aim to form different configurations: it can be either shaped in a configuration that fits the liquid container in which it should be installed, it can be packed in blocks, rolled in cylindrical shape or also reduced to small cylinders (pellets).
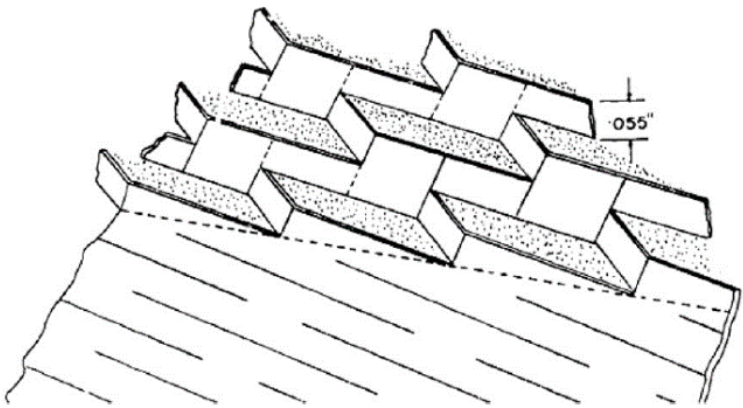
Figure 15 – Sketch of Explosafe production process: slit and expansion of a small thickness aluminium foil [13]

(a)   (b)

Figure 16 – Explosafe cylindrical block used in the present thesis's tests.

Once placed inside a tank, Explosafe only takes up 1-3% of the tank volume.

All the tests presented in this thesis have been performed using a cylindrical shaped block of Explosafe that perfectly fitted the experimental tank, kindly offered by Explosafe Limited of Switzerland . Single layers were rolled in order to match precisely the internal diameter of the tank, and then inserted inside the cylinder. The filler was specifically targeted to grant contact with all the tank's internal surfaces.

Figure 17 – Frontal view of Explosafe
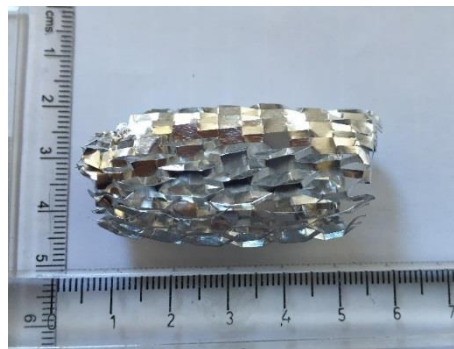
Figure 18 – Explosafe small cylindrical pellet, as furnished by Explosafe Switzerland for tests at Politecnico di Milano facility.

Figure 19 – Explosafe small cylindrical pellets configuration

2.2   Ballistic tests

Ballistic tests were performed at the Laboratorio Sicurezza Trasporti (LaST) of the Aerospace Science and Technology Department (DAST) of Politecnico di Milano. The projectiles were spherical steel balls with different sizes (up to 16.6 mm diameter). They were accelerated up to 180 m/s with a compressed air device.

The acceleration system was designed and built at the Politecnico di Milano some years ago, and it was also employed in previous thesis involving self-healing materials. The system is able to reach velocities up to 240 m/s [20], but in the present thesis only velocities around 180 m/s were reached because of research requirements definitions.

Diameter [mm]	Mass [g]
2.35	0.053
3	0.110
5	0.511
6.34	1.041
8	2.091
10	4.084
12	7.057
14.27	11.868
16.6	18.740

Table 3 –Steel spheres' mass
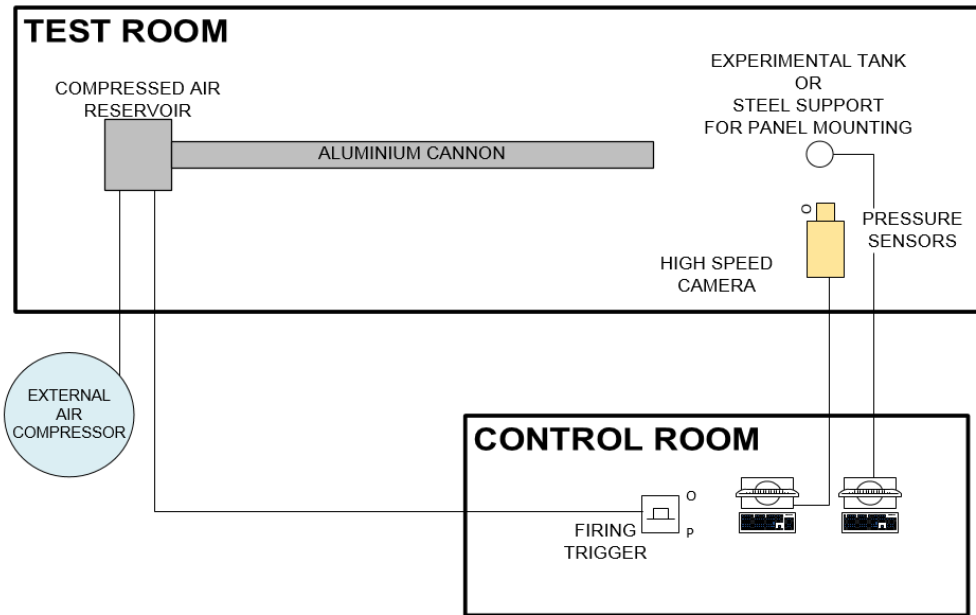
Figure 20 – Politecnico di Milano (LaST) experimental facility

The acceleration equipment is composed of a chamber pressurized by an external compressor (pressure up to 8 bar can be reached, but in order to obtain a projectile speed of 180 m/s, a pressure of 6.5 bar was enough) and separated from the outside ambient through a 0.075 mm thick golden foil. An electronic switch activates a solenoid that is able to move an iron trigger with a sharp point toward the golden foil.
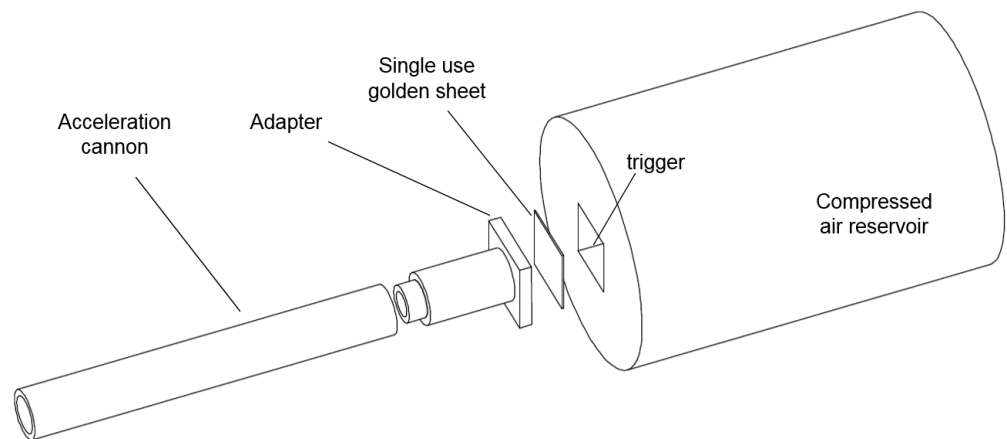
Figure 21 – Detailed view of cannon's base attachment. Sabot is inserted inside the barrel between the adapter and the acceleration cannon.

Figure 22 – trigger

After the puncture, the differential pressure causes the expansion of the compressed air in a long aluminium tube (length 7 metres, internal diameter 40 mm, external diameter 70 mm). The air expansion pushes a high density polyethylene (HDPE) sabot, which contains the selected size steel sphere inside the aluminium tube till it reaches the end of the barrel, made by a dissipative small thickness aluminium tube (absorber) and an aluminium stopper (a sort of cover cap). This terminal part was recently modified in its design in order to facilitate the recharging operation and it is more accurately described in §2.2.1 .
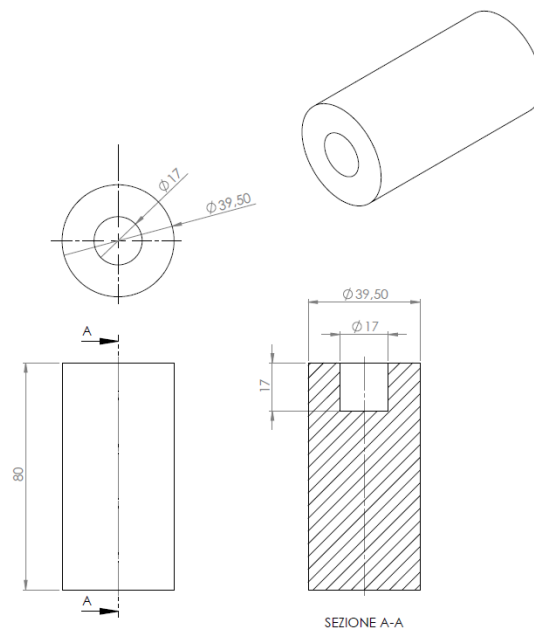
Figure 23 – Sabot technical drawing

Figure 24 – sabot end-run stopper and absorber

A high velocity Phantom v5.1 camera was used to measure the projectile's speed before and after the impact by computing the time elapsed by the projectile to cover a fixed distance.

Figure 25 – Phantom v.5.1 high speed camera

Positioning of the ionomer was dependent on the kind of tests done (i.e. in air or in the water environment). In the former case, ionomer specimens were installed on a steel rigid support. The frame was anchored to the ground by four M6 bolts and the L shape of the beam section guarantees a lower deflection of the structure during the impact. In this thesis, the support's option of varying the inclination of the specimens with respect to the panel motion was not exploited.

In the case of tests performed with the tank, the steel frame was removed and the ionomer panel was part of the entry wall of the tank itself. The experimental tank was

specifically designed for this experimental campaign, and accurate description of the trade-off and design process is reported inside §2.2.2 .

Figure 26 – steel support used for tests in air environment

2.2.1 Acceleration module modifications

Before starting the experimental campaign, modifications to the experimental facility have been carried out. A new barrel closure module has been designed under the main requirements of one person operation and easy stopper and sabot removal.

In fact, in the past configuration, at least two people were necessary in order to operate the sabot removal. After every shot, one operator should lift the aluminium tube in the part near the pressurized reservoir, and the other should use a 10m-long thin steel pole in order to pull the sabot out the frontal exit of the tube.

That operation should be done after the opening of the stopper through 4 transversal M8 bolts. In fact, the sabot remained inside the tube (about 10 to 15 cm from the exit), and cannot be removed by extraction from the exit side.

The new system allowed the sabot extraction without lifting the 7-meter long aluminium tube and even without unscrewing the four stopper's bolt. Only a simple operation of unscrewing the entire terminal part shall be done in order to retrieve the sabot. Every 2 to 4 shots, also the aluminium dissipative tube shall be replaced after the unscrewing of four M8 stopper bolts. This aluminium tube dimensions have been

chosen in the past as 28 mm and 26 mm for external and internal diameter respectively. A new choice of 28/25 mm was done, thus augmenting the cylinder thickness from 1 mm to 1.5 mm.
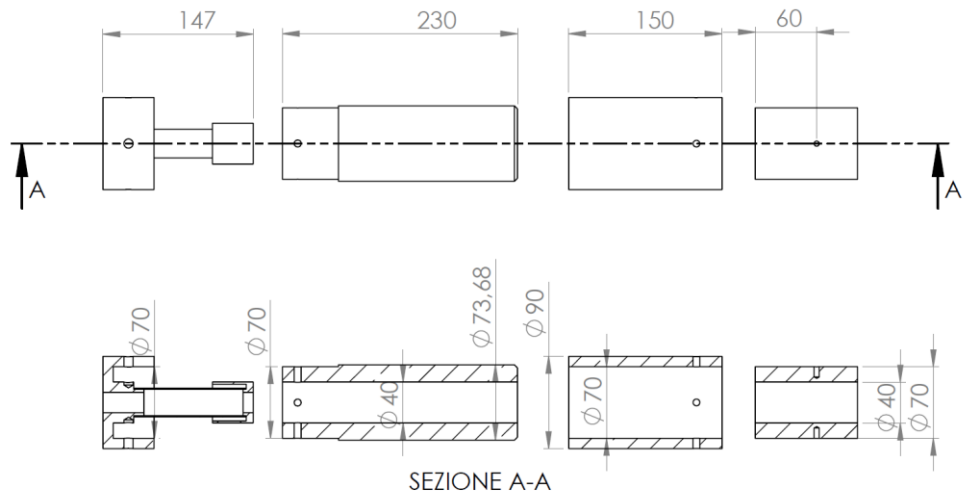
Figure 27 – Technical drawing of acceleration cannon terminal part
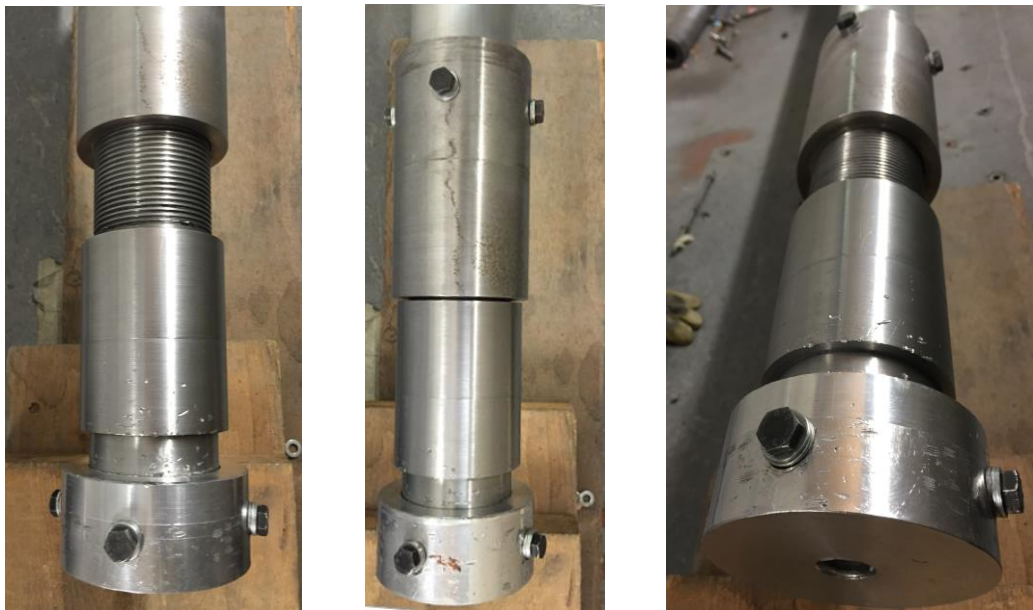
Figure 28 – Photographs of the terminal part of the acceleration cannon

The new system has been tested in the present thesis with more than 70 shots and can be considered a validated configuration. Its larger section provided a longer durability, but on the other hand the sabot was subjected to a higher stress. Sabot replacement was thus needed after around 25 shots.

A further modification that could be done is a fast-removal barrel stop cover, implementing a similar system to the just presented one. In fact, in the present system, transversal bolts are subjected to high stresses and need replacement after 10 to 15 shots. Alternatively, M8 bolts can be replaced by four M10 bolts in order to increase robustness of the part.

2.2.2 Tank

The novelty of this thesis work was ionomer testing in contact with water. A new tank is thus designed and built, starting from some main requirements:

- The tank shall be compact enough to be easily moved by one person only at full capacity;
- The tank shall be able to withstand the forces arising from a maximum of 16.6 mm spherical steel bullet at 200 m/s.;
- The tank shall be predisposed to pressurization;
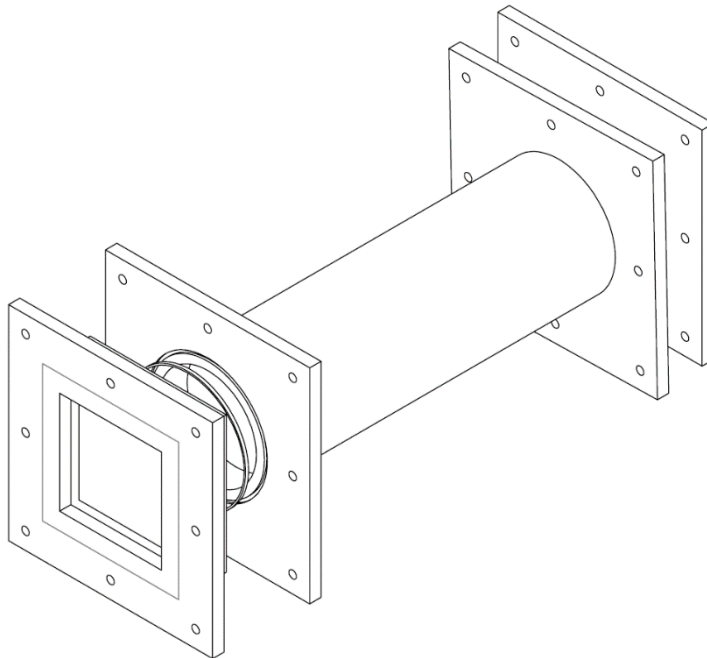
Figure 29 – Sketch exploded view of the experimental tank.

- The ionomer panel shall be easily changed in few minutes, without the need to remove the liquid inside the tank;
- At least for some tests, the ability to see inside the tank shall be granted;
- The tank shall be predisposed to pressure sensors installation.
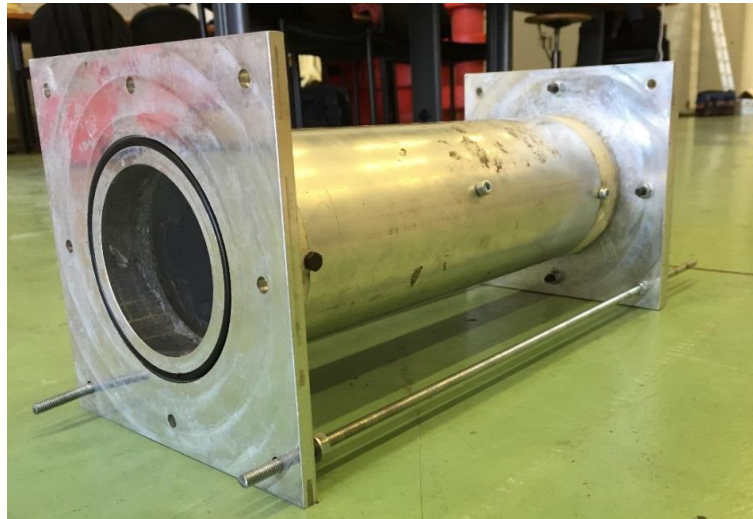
Figure 30 –Entry side tank view.

The design phase brought to a cylindrical shaped tank, with an internal diameter of 92 mm, a length of 366 mm and an approximate volume of 2.4 litres.

The specimen was clamped on one base of the cylinder by a square flange with a hole of diameter 86 mm.

In order to satisfy the requirement of having the possibility to observe inside the tank during (and after) the impact, there was the possibility to interchange the aluminium cylinder with a Plexiglas one. The system is clearly more fragile, but had the remarkable advantage of permitting to see inside the tank. However, perfect visibility in zone just after the impact was not permitted by the chosen design of the flanges. The driving motivation was to guarantee a higher resilience to stress derived from the impacts.

The matching between the cylindrical shape and the flanges guaranteed a minimum clearance space. Sealing was obtained by adding a silicon glue at contact points.

Aluminium flanges separation from the central cylinder was prevented by four long steel screws.
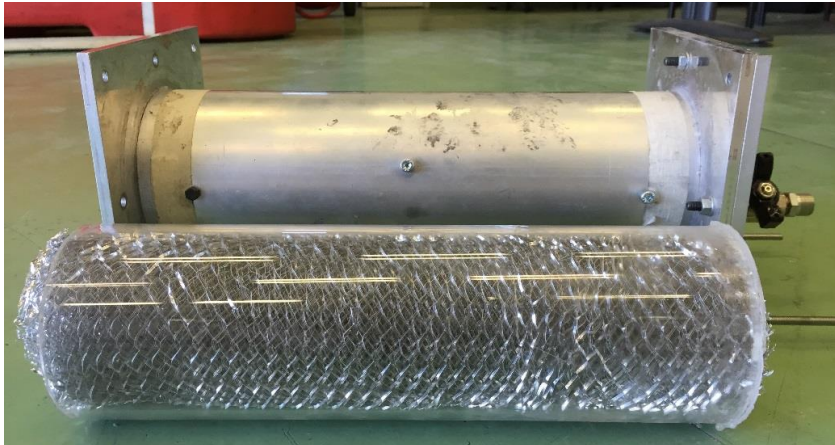
Figure 31 –Lateral view of the two different tank configurations put aside. The plexiglass cylinder in the photograph is filled with Explosafe, but tests without the filler have been performed too.

Figure 32 – Explosafe frontal view inside the tank (without and with ionomer panel respectively)

Figure 33 – Explosafe insertion phase inside the experimental tank.
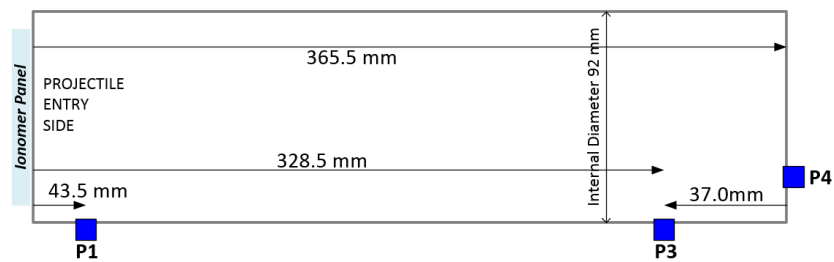
Figure 34 – Pressure sensors position

The twin flanges were a critical part in the mechanical project of the tank. They were obtained from a single aluminium block by a numerical controlled milling-machine. Operations and material for the two twin flanges has been kindly offered by Fratelli Ronchetti [21].
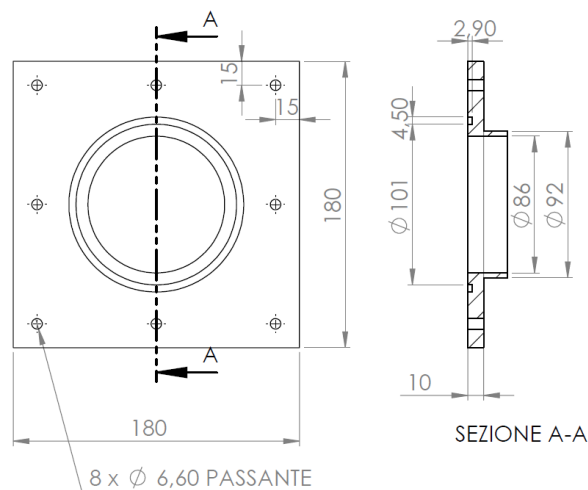
Figure 35 – Technical drawing of the flange, a critical part of the tank.

2.3   After impact analysis

After testing, all specimens were photographed with a classical camera, in order to show morphological features of the impact zone.

In addition, scanning electron microscope (SEM) allowed an analysis at a smaller scale both in the bullet entry and exit sides. A Hitachi TM3000 instrument was employed.

Figure 36 – Scanning Electrons Microscope in use at Politecnico di Milano laboratory.

To check the healing of the panel, leakage tests were carried out using a vacuum pump and a procedure inherited from the previous thesis works at Politecnico di Milano. The pump was applied on one side of the specimen with a pressure difference of 0.9 bars. Air tightness through the hole was tested following vacuum decay.

In case of healed hole, a weak vacuum decay was detected within a specified time range (10 min), whereas for non-healed samples vacuum decay was always observed within one minute.

In the case of testing in the tank configuration, water passage through impact zone was checked before operating the air leakage test just described.

Figure 37 – Leakage test instrument.

3.   EXPERIMENTAL:
ballistic tests at low speed

Experimental tests have been carried out in three different configurations at a fixed projectiles' velocity of 180 m/s. Therefore, the variable parameters are the panel thickness (s), the projectiles' diameter (d) and the test configuration. The latter are, as already mentioned, of three different typologies:

- ionomer in air environment;
- ionomer in contact with water, also referred to as *tank* configuration;
- ionomer in contact with water, with Explosafe® inside the tank (*Explosafe configuration*).

Parameter	Description	Abbreviation
Velocity	180 (±5) m/s	Low
Configuration	air, water, water and Explosafe®	
Panel thickness	1.5, 2, 3 mm	s
Projectiles' diameter	from 5 to 16.6 mm	d
Specimen	Surlyn® 8940 ionomer (stand-alone configuration)	S8940

Table 4 – Experimental set conditions

3.1   Tests in air environment

3.1.1   Experimental strategy and results' table

Surlyn®8940 healing capabilities have been already studied by S. Coppi [4]. Her set of data, coming from 9 tests, is reported in Table 5 for sake of convenience.

A total of 8 similar tests have been conducted in this thesis for different thicknesses, in order to extend the dataset (Table 6).

Experimental strategy emulated the one followed in Coppi's Master thesis, consisting in keeping the velocity parameter fixed and changing other variables such as panel thickness (s) and spherical projectiles' diameters (d).

S	d	s/d	V imp [m/s]	V res [m/s]
0.6	3	0.20	173	167
0.6	2.35	0.26	172	147
0.6	5	0.12	183	165
1.02	5	0.20	184	177
1.02	3	0.34	190	175
1.86	5	0.37	185	155
1.86	6.34	0.29	182	155
1.86	8	0.23	178	150
1.86	10	0.19	185	159
2.62	10	0.26	178	150
2.62	8	0.33	185	150
2.62	12	0.22	185	158

Table 5 – Experimental ballistic data outlook of S. Coppi's thesis [4]

Panel ID	s [mm]	d [mm]	s/d	V imp [m/s]	V res [m/s]
151_1	1.5	7	0.21	197.03	140.11
152_1	1.5	8	0.19	180.15	93.41
207_1	2	8	0.25	191.06	124.55
206_1	2	10	0.20	176.27	116.76
205_1	2	10	0.20	195.16	120.10
306_1	3	16.6	0.18	182.15	123.63
305_1	3	14.3	0.21	195.16	123.63

Table 6 – Experimental ballistic data outlook of the present thesis

3.1.2 Healing morphological analysis

3.1.2.1 Visual

The first evidence of healing was from a visual analysis: the spherical projectile perforated the ionomer panel but the impact region did not always present a hole. The passage area was closed, though leaving a permanent deformation and clear evidence of a damage event.

The closure pattern presented some petals, probably generated from the cracks geometry during the impact. The contemporaneity of the elastic return with the solidification of the molten ionomer granted the sealing of petals, which generally were no more than three.

The petals' region did not extend to the complete footprint of the sphere's diameter: it encompassed only an inner part.

The surrounding region presented a bulking region on the backside of the panel. In this region, visible crack were never registered. The outer border represented the projectile's diameter approximately. Outside the range given by that diameter, in fact, no remarkable sign of modification was never found.
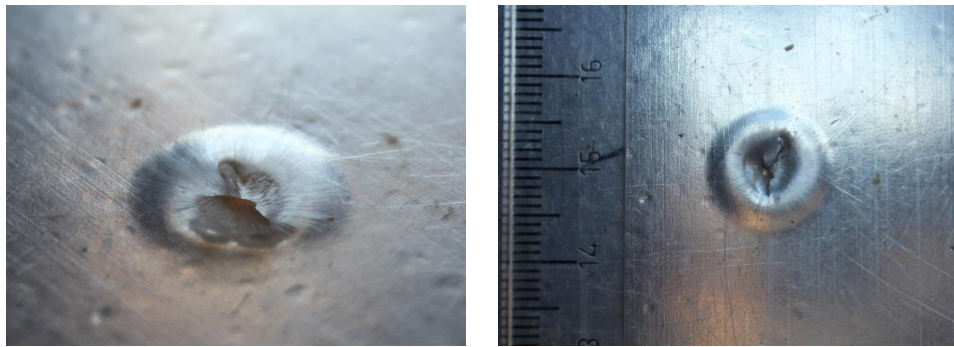
Figure 38 – Panel 306

Figure 39 – Panel 210

3.1.2.2 Leakage test and hole measurement

Leakage tests' graphical results are reported in Figure 40. The behaviour of the repaired panels were similar, and sometimes they were graphically superposed. Not perfect leakage behaviour was imputed to be a cause of the experimental system used. However, results were comparable to the previous thesis, and thus in case of less than 10% pressure reduction in 10 minutes, the panel was considered to be repaired.
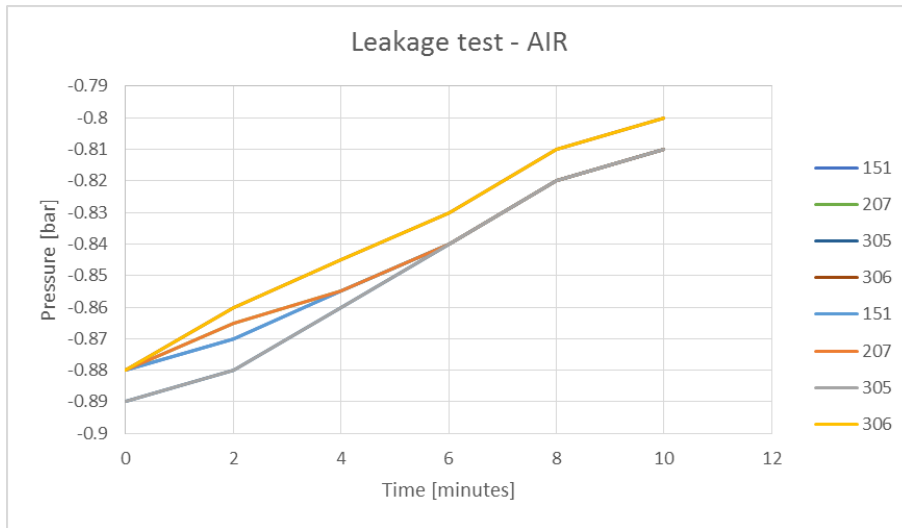
Figure 40 – Leakage tests for panels in air environment

In addition to the classical leakage tests, hole measurements after projectile passage have been done with a traditional calibre. The aim was to create a sort of healing map for partial hole closure, in a similar way to what is done in the study of other classical materials behaviour (e.g. for aluminium plates is important the number of petals, or the ejection of fragments [22]). This operation should be useful for a further numerical code development. Results are presented in the following table.

Non repaired cases only are showed. Diameter of the hole was not always under 1mm. However, at least a 50% reduction in hole's diameter was always found. In fact, the two "false" cases had a diameter of about 2 mm.

Panel ID	s [mm]	d [mm]	s/d	AIR LEAKAGE	RESIDUAL HOLE < 1mm
206_1	2	10	0.20	True	False
152_1	1.5	8	0.19	True	False
205_1	2	10	0.20	True	True
206_1	2	10	0.20	True	True

Table 7 – Residual hole measurement after projectile passage, in air environment.

3.1.3 Ballistic tests' discussion

3.1.3.1 S/d ratio

Once reparation was tested, results were summarized in the s/d ratio table, already proposed previously and used as reference in all other thesis work and articles developed inside the Politecnico di Milano' s research programs [4] [20] [23] [24].

Table 8 reports all the results obtained for Surlyn®8940 testing in air environment, at low speed. Green cells indicate conditions where healing has been verified, while for red ones there was air leakage. White cells represent conditions where the reparation behaviour has not been verified yet.

s \ d	2.35	3	5	6.34	7	8	10	12	14.3	16.6
0.6	0.26	0.20	0.12	0.09	0.09	0.08	0.06	0.05	0.04	0.04
1	0.43	0.33	0.20	0.16	0.14	0.13	0.10	0.08	0.07	0.06
1.5	0.64	0.50	0.30	0.24	0.21	0.19	0.15	0.13	0.11	0.09
1.86	0.79	0.62	0.37	0.29	0.27	0.23	0.19	0.16	0.13	0.11
2	0.85	0.67	0.40	0.32	0.29	0.25	0.20	0.17	0.14	0.12
2.62	1.11	0.87	0.52	0.41	0.37	0.33	0.26	0.22	0.18	0.16
3	1.28	1.00	0.60	0.47	0.43	0.38	0.30	0.25	0.21	0.18

Table 8 – S/d ratio healing table in air environment, at 180 m/s.

With the available data set, a new graph has been created (Figure 41). The green line represents the second order polynomial interpolation for the most critical healing condition of a given thickness (i.e. at a given thickness, the green cell positioned on the foremost right in the s/d ratio table), while the red line represents the non-repaired condition nearer to the repaired condition. In fact, the aim of these tests was to highlight the *reparation limit*, which is summarized by the blue line. That blue line mathematically represents the interpolation (always a second order polynomial, in this case) for all the limit conditions, that is for all the set of green and red points that are presented in the graph.

This graph represents a more immediate instrument for the comparison of different scenarios and also an alternative way to express the data until now reported only by tables.

Although the chosen interpolation line is of second order instead of a classical straight line, it is not so distant from the value of s/d equal to 0.20. A slight improvement in the performance, that means a decrease of this ratio (e.g. for the same bullet diameter, it is enough a smaller thickness of the panel in order to have healing), started to appear

for higher thickness of the panel. Unfortunately, the testing facilities did not permit tests with bullet calibres higher than 16.6 mm. This means that a non-healing condition could not be found for the 3mm-thick panel.
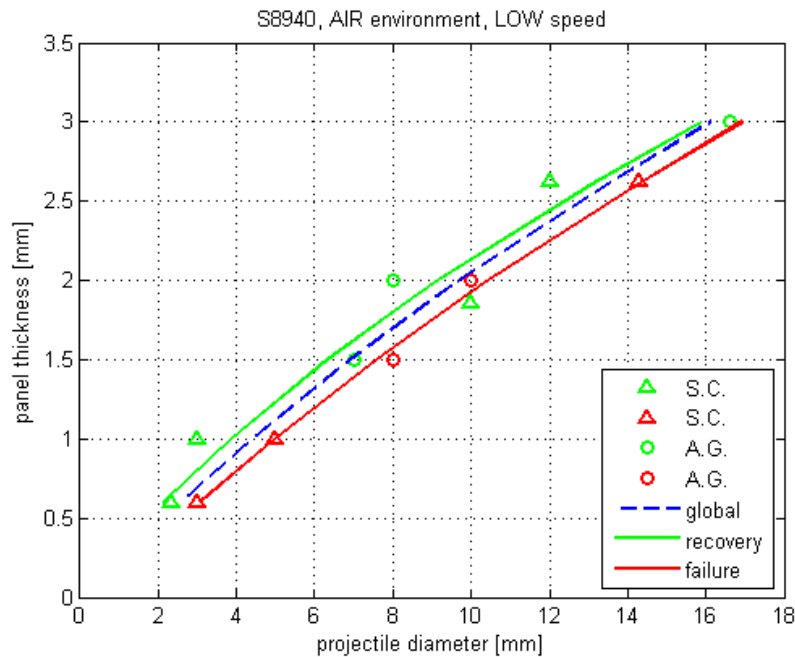
Figure 41 – s/d limit graph in air environment (2nd degree polynomial interpolation)

3.1.3.2 Energy considerations

The s/d ratio is, until now, the only affordable characteristic parameter that is able to discriminate between reparation and non-reparation of a panel. It is a parameter of pure geometrical nature, but also energy is likely to have an important role in the determination of healing, since it is through energy exchange that the panel is locally melted and deformed.

With the aim of trying to find a characteristic relation linked with energy, the following dissertation is presented.

In fact, the starting point in all types of ballistic studies of this kind is the dissipated energy, i.e. the energy lost by the projectile during the impact and thus acquired by the panel ([25], [22]). In order to compute the dissipated energy, it is enough to find the kinetic energy variation of the projectile. It is that fraction of energy that is transformed

in heat (governing the ionomer local temperature) or in elastic and plastic deformation of the panel.

The kinetic energy difference was computed from the ballistic experimental data (velocity before and after the impact were recorded with the high speed camera) as the arithmetic difference between the kinetic energy of the sphere before and after the impact.

s/d	Air leak.	V_{impact} [m/s]	V_{res} [m/s]	Mass [g]	A_{imp} (e-5) [m2]	Ek_in [J]	Ek_fin [J]	ΔE [J]	ΔE/A [J/mm²]	ΔE/V [J/mm³]	ΔE/m [J/kg]
0.6/3	T	173	167	0.11	0.71	1.7	1.55	0.11	0.02	0.03	13945
0.6/2.35	F	172	147	0.06	0.43	0.9	0.63	0.23	0.05	0.09	10805
0.6/5	T	183	165	0.51	1.96	8.6	6.96	1.60	0.08	0.14	13613
1/5	T	184	177	0.51	1.96	8.7	8.00	0.65	0.03	0.03	15665
1/3	F	190	175	0.11	0.71	2.0	1.70	0.30	0.04	0.04	15313
1.86/5	F	185	155	0.51	1.96	8.7	6.14	2.61	0.13	0.07	12013
1.86/6.34	F	182	155	1.04	3.16	17.3	12.54	4.75	0.15	0.08	12013
1.86/8	F	178	150	2.09	5.03	33.1	23.54	9.61	0.19	0.10	11250
1.86/10	F	185	159	4.09	7.85	70.0	51.66	18.28	0.23	0.13	12641
2.62/10	F	178	150	4.09	7.85	64.8	45.98	18.77	0.24	0.09	11250
2.62/8	F	185	150	2.09	5.03	35.8	23.54	12.26	0.24	0.09	11250
2.62/12	F	185	158	7.06	11.3	121	88.12	32.69	0.29	0.11	12482

Table 9 – Energy computation table for previous experimental data.

ID	Air leak.	V_{impact} [m/s]	$V_{residual}$ [m/s]	Mass [g]	A_{imp} (x10⁻⁵) [m²]	E_{k_in} [J]	E_{k_fin} [J]	ΔE [J]	ΔE/A [J/mm²]	ΔE/V [J/mm³]	ΔE/m [J/kg]
151	F	197.03	140.11	1.04	3.85	20	10	10	0.26	0.17	9815
152	T	180.15	93.41	2.09	5.03	34	9	25	0.49	0.33	4362
207	F	191.06	124.55	2.09	5.03	38	16	22	0.44	0.22	7756
206	T	176.27	116.76	4.09	7.85	63	28	36	0.45	0.23	6816
205	T	195.16	120.10	4.09	7.85	78	29	48	0.62	0.31	7212
306	F	182.15	123.63	18.74	21.6	311	143	168	0.77	0.26	7642
305	F	195.16	123.63	11.87	16.1	226	91	135	0.84	0.28	7642

Table 10 – Energy computation table for present thesis experimental data.

The first step was to plot the dissipated energy as function of the panel thickness (Figure 42). This operation has been already done in previous thesis.

First of all, it is necessary to underline that the sphere's diameter was not a constant, neither in the x axis nor in y axis set of tests. For example, the two circles for the 2 mm panel are made with spherical projectile of 8 and 10 mm, while the circles for the 3mm-thick panel were coming from tests with 14.3 and 16.6 projectile diameters. This is because the tests' main driver was always the s/d ratio, and experiments were primary targeted to investigate that reparation behaviour.

A global tendency highlighted from the graph is that the non-reparation events were characterized by a higher value of dissipated energy. It seemed that the more energy was absorbed by the panel, the more difficult the panel reparation was.

According to this consideration, from the physical point of view, the panel supported a higher stress, and its local temperature rise was too high.

Perhaps the region that experienced a high temperature was too large, and the deformation was too high to guarantee an elastic return.
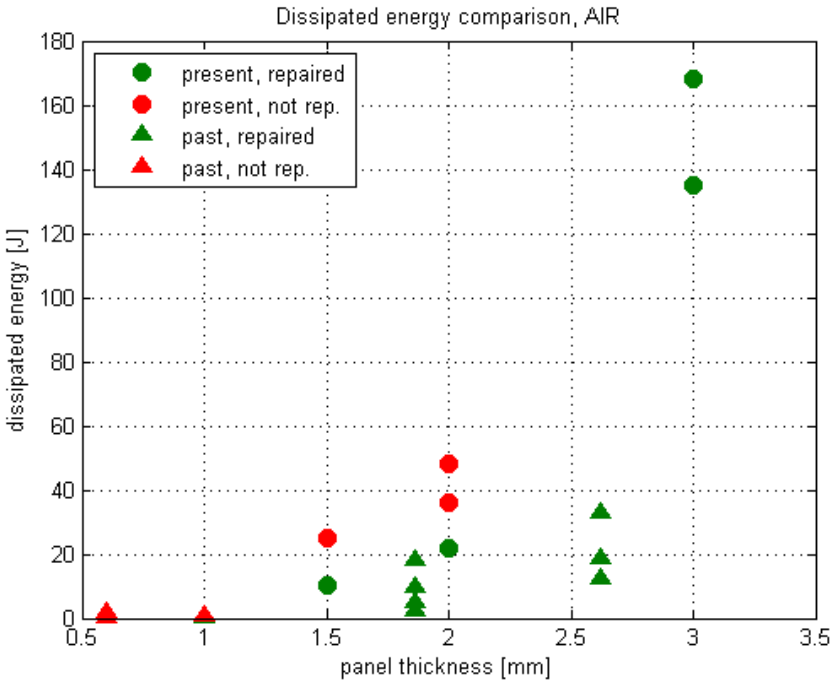
Figure 42 – dissipated energy graph for pure Surlyn8940 in air environment
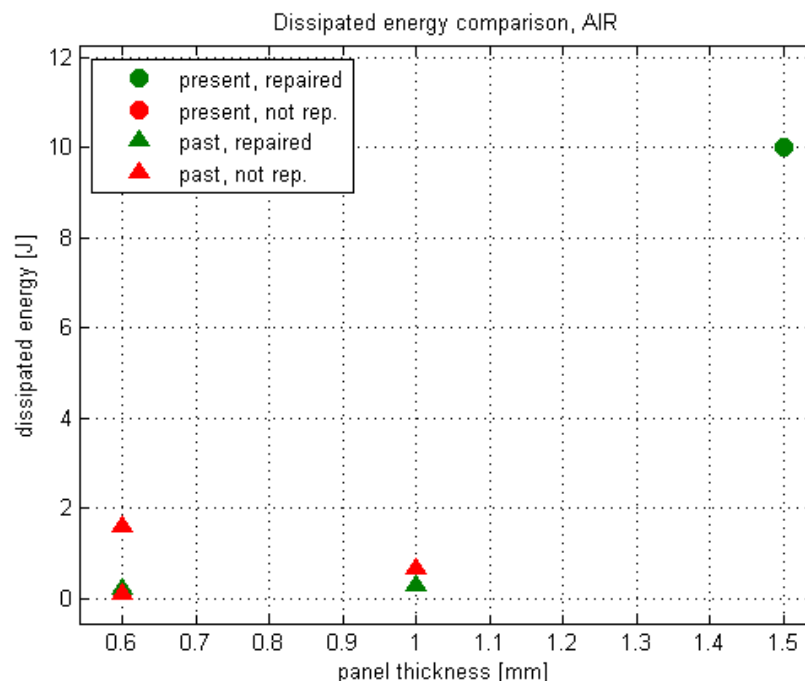
Figure 43 – Dissipated energy graph for S8940 in air (magnification)

Data gathered from past works and the present one, showed the same tendency but a translation too. The motivation should be accounted to some differences in the material or in the panel production process. However, the most important aspect is the general trend: as panel thickness increased, dissipated energy increased too.

Actually, according to the projectile diameter, the mass of the sphere and the impacting area on the panel changed too. This consideration was the driver for a new way of representing data from the tests, in which some novel parameters have been introduced: the dissipated energy over the cross-section area of the impacting sphere, the dissipated energy over the *displaced* volume (intended as the product of the cross sectional area of the projectile and the panel thickness) and the dissipated energy over the projectile mass. In the dissertation of energy over the area, some other correlated ways of considering the area will be proposed and discussed.

For what concerns the normalization with respect to the *impact area*, i.e. the cross section of the sphere, results have been plotted in Figure 44: the dissipated energy (joule) per unit area (mm²) was expressed as a function of the panel thickness.

Tendency had now a linear trend, instead of an exponential one. Non repaired panels were still positioned in the upper part of the graph for the higher thickness panels, while for 1 and 0.6 mm panels, more ambiguity is present because of superposition of results.
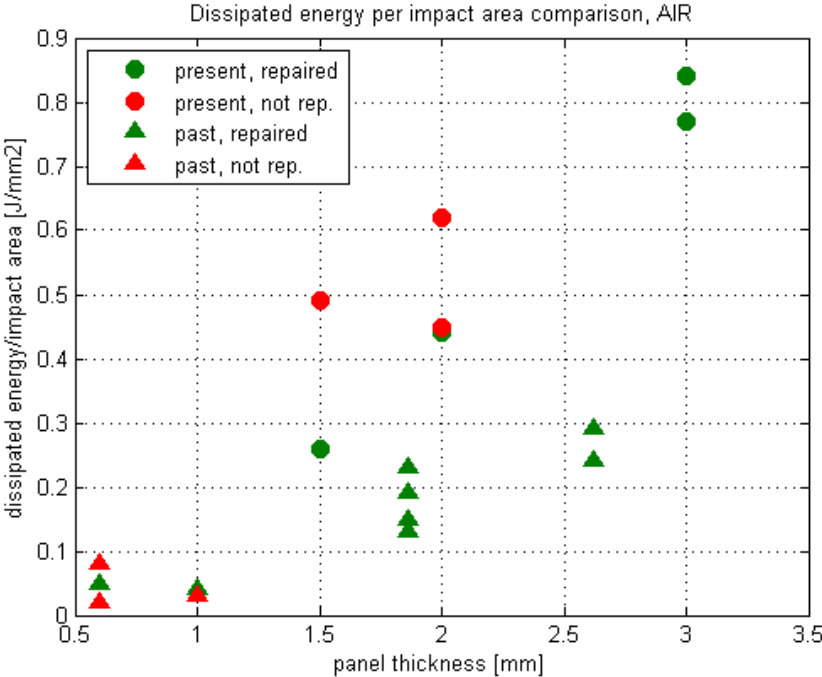
Figure 44 – Dissipated energy per impact area for S8940 in air

Differences between the data of the present thesis and the ones by previous ones still remained, but the trend was confirmed.

A consideration that is possible to derive from the graph is about the elastic behaviour of the material: the panel with larger thickness had a different deformation response. The thicker the panel, the larger the energy that the panel was able to subtract to the projectile, no matter of its areal density.

However, in order to cancel completely the relationship of the mass on the computation of the variation of the kinetic energy, there is the necessity to normalize the variation of the dissipated energy with respect to the mass or the volume of the sphere. The idea of using the impact are was due to the idea of distributing the

dissipated energy on the surface that is more exposed to friction (and then to consequent heating and melting).

Before proceeding to the mass and volume discussion, in the following two graphs, an implementation of the division by the area concept has been done by using the lateral area of a cylinder with base the impact area and height the thickness of the panel (called *tunnel* surface for sake of simplicity) and the tunnel area plus half of the area of the steel sphere impacting the panel (that is the *bow surface* that was in contact with the ionomer during the perforation).

The main driving idea was to try to correlate the energy no more with the frontal area of impact, but with two areas through with there is the contact (and then friction) between the impacting sphere and the ionomer.

Results of these two normalizations are represented in Figure 45 and Figure 46. It is possible to observe a very similar behaviour to the ones obtained with the cross sectional area, but some additional separation between some red and green points is visible. Red and green points on 1.5 and 2 mm panel thickness continued to show a sort of critical value that can discriminate healing.
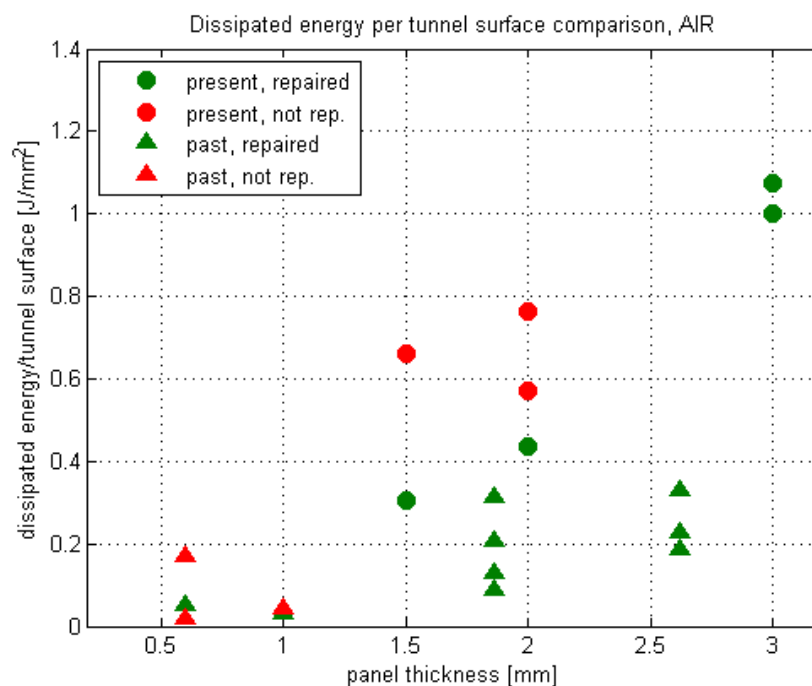
Figure 45 - dissipated energy per tunnel surface for S8940 in air
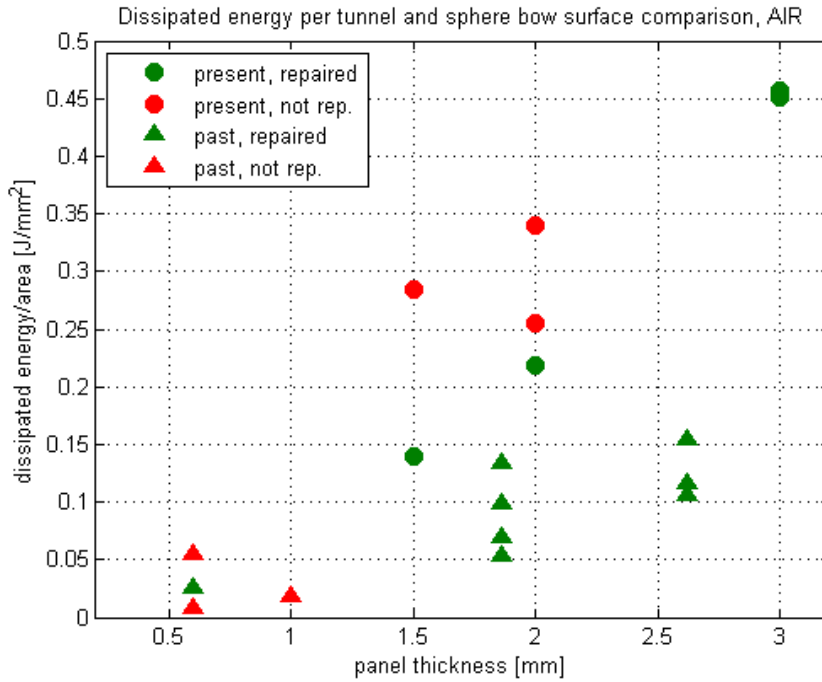
Figure 46 – Dissipated energy for tunnel and bow area.

The next step was to check the behaviour in the case of a volume obtained by the product of the cross section of the sphere and the thickness of the panel. In this case, represented in Figure 47, all points distributed around the same medium value. There was still a discrepancy between the values by past works and the ones of the present thesis, but it is possible to observe that the possibility to identify a critical value of $\Delta E/V$ valid for all tests was approached.

In addition to that critical value identification, the spreading of the dissipated energy on the volume allowed some rough preliminary computations on the value of temperature that the panel could experience.

From the energy equation, $\Delta E = mc_p\Delta T$, it is possible to rewrite the expression in a more convenient way: $\Delta E/V = \rho c_p \Delta T$. By substituting the known numerical values for ionomer density (0.95 g/cm^3) and specific heat (approximated 1000 J/kgK), it is possible to compute the variation of temperature once the energy value is known. Considering values from 0.05 to 0.35 J/mm^3, expected temperature variations are from 50 to 350 K (or °C). A temperature variation of 50°C means a heating up to about 75°C, not enough to reach the melting point of the material (fusion is at 96°C), and from the graph it is possible to see that reparation was more difficult. On the contrary,

for presumed temperature variations, consistent with material melting, reparation was always verified, until becoming more difficult for higher values.

It is worth remembering that the volume value is a rough approximation, since the area around the impact footprint is likely to be heated up too. The considerations that drove that division was essentially the footprint left by the sphere, since, by visual analysis, it was the only one that was subjected to a phase change.

Another element that is dissipating energy is the permanent deformation of the panel, which in some cases could be noted even by visual inspection.

Literature is not completely in agreement with temperatures during healing, and to now data are still quite poor in number. Thermal imaging could be the definitive way in order to attempt a correlation of this theoretical computations with reality.
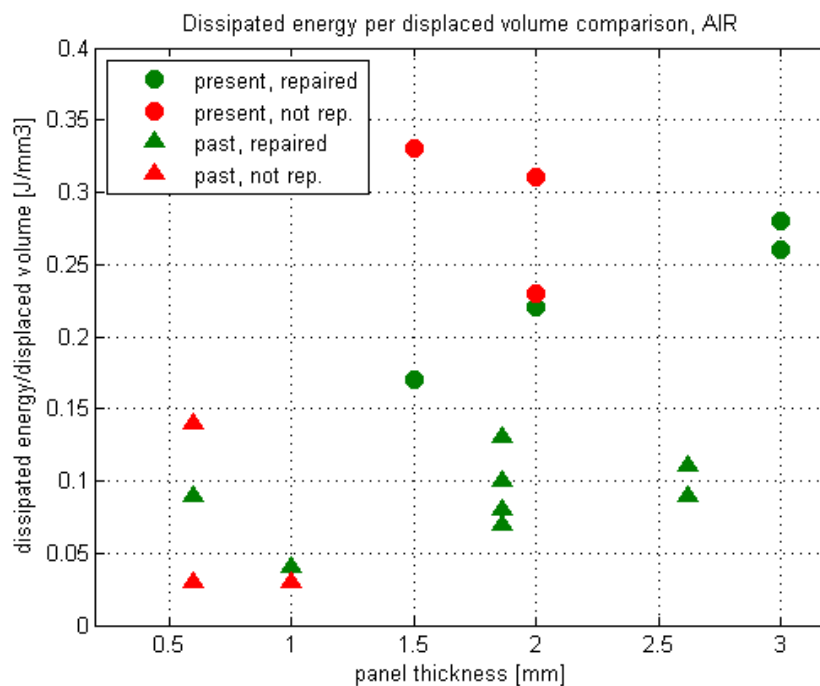
Figure 47 – Dissipated energy per impact area multiplied by panel thickness for S8940 in air

In conclusion, a graph with normalization with respect to the mass of the projectile has been developed too. Results are quite similar to the ones described on $\Delta E/V$, even if they were subjected to a symmetrical inversional.
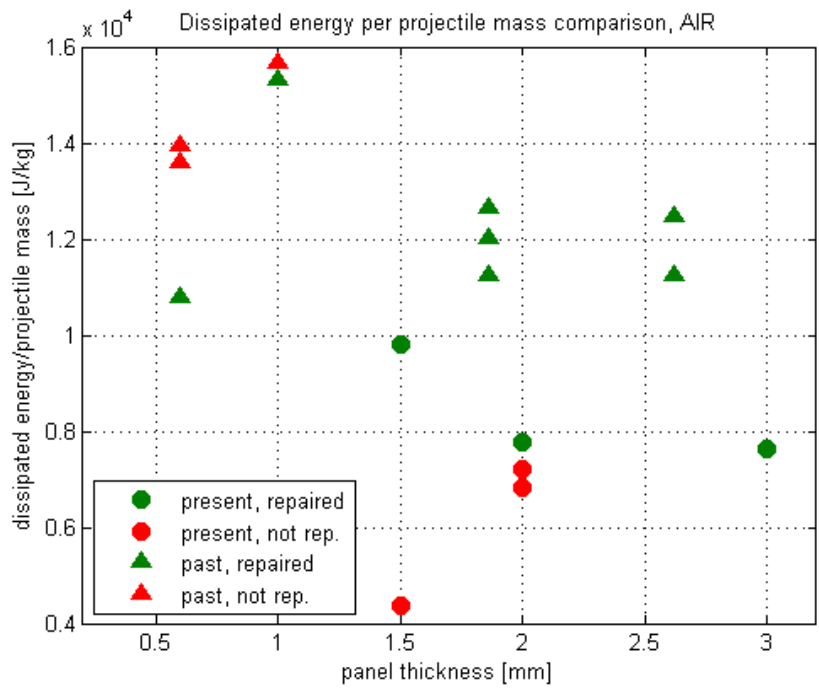
Figure 48 – dissipated energy per projectile's mass for pure Surlyn8940 in air environment

3.2 Tests in air-water environment (tank)

3.2.1 Experimental strategy and result's table

A number of tests were done in a Plexiglas cylinder configuration with the objective to have visibility inside the tank during the impact.

Unfortunately, the configuration did not allow to see perfectly the back side of the panel (i.e. the wet part of the panel). This limitation was known, and discussed also in the design phase of the experimental tank.

After taking some measurements, experiments continued with the aluminum cylinder for another dozen of tests. The choice was driven by some ruptures in Plexiglas. Aluminium configuration was obviously more resistant and also allowed to place pressure sensors inside the tank.

The drawback was the complete loss of info about the mean projectile velocity on its track inside water.

3.2.2 Healing morphological analysis

3.2.2.1 Visual

Visual analysis showed immediately some differences in the morphological pattern left by the projectile passage: in the majority of cases, petals' presence was not evident. The fused ionomer showed an axial-symmetric solidification of the fused part. In fact, with respect to the central axis of the hole, axial-symmetry was a considerable novelty of this water configuration. It was then possible to suppose that the water, with its pressure acting in the opposite direction with respect to the bullet motion, physically supported the elastic return in a more homogeneous way. Unfortunately, videos of this phenomenon were not available because of the blind region due to the flanges' geometry.

Cracks and *petalling* in the ionomer were not a routine trend, but the majority of the tests showed some stripes in the entry side.

A bulking region outside the inner circle area of the impact was present also in this case. No evidence of modification in the ionomer on a region larger than the cross section of the impacting object was found.

Also in the water case, even when the panel reparation was not complete, the hole reduction was substantial. Panel 204 is a paradigmatic case of regions division and small residual hole even if reparation failed.

Panel 159
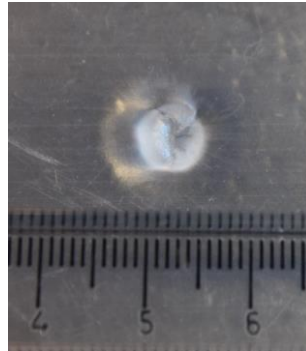
Panel 202
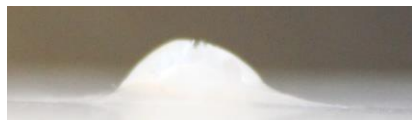
Panel 202
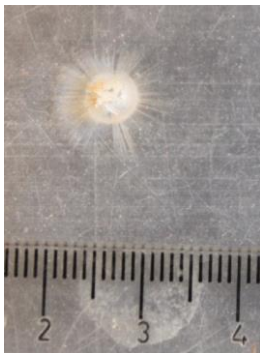
Panel 203

Panel 204
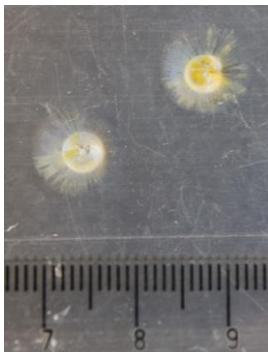
Panel 302
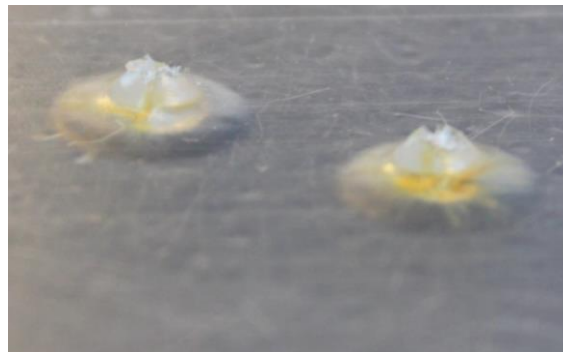
Panel 303

Figure 49 – Photographs of different panels tested in water environment

3.2.2.2 Leakage tests

Panel ID	s [mm]	d [mm]	s/d	WATER leakage	AIR leakage	RESIDUAL HOLE < 1mm
153	1.5	12	0.13	True	True	False
303_1	3	12	0.25	False	True	True
303_2	3	14.3	0.21	False	True	True
204	2	16.6	0.12	True	True	False
154	1.5	10	0.15	True	True	True
159	1.5	8	0.19	True	True	True
156	1.5	6.34	0.24	False	True	True
301	3	10	0.30	False	False	
302_1	3	10	0.30	False	False	
302_2	3	10	0.30	False	False	
201_1	2	10	0.20	False	False	
201_2	2	10	0.20	False	False	
201_3	2	10	0.20	False	False	
202_1	2	12	0.17	False	False	
303_1	3	12	0.25	False	False	
303_2	3	14.3	0.21	False	False	
203_1	2	12	0.17	False	False	
203_2	2	14.3	0.14	False	False	

Table 11 - Leakage tests results for water environment tests

The first observation on healing performance was possible just after the impact: some panels showed water spillage, while others did entrain water inside even if they did not show complete reparation in further analysis with the classical air leakage test.
This peculiar behaviour extends the benefits in possible applications concerning water spillage prevention.
Air leakage tests results were grouped in Figure 50.
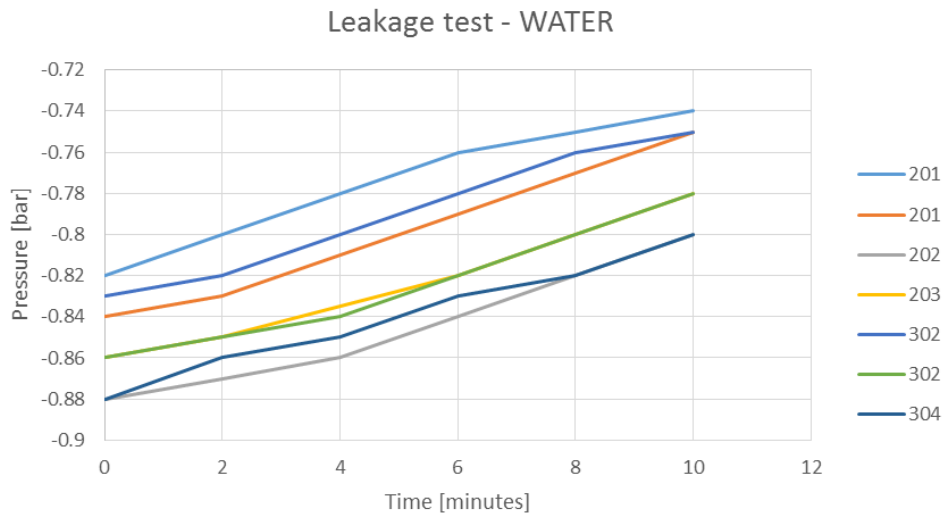
Figure 50 – Leakage tests for panels tested in water environment

3.2.2.3 SEM

Analysis with the Scanning Electron Microscope showed some novelties with respect to the previous experimental campaigns. Agglomerates were evident in all analysed panels and they were positioned in the melted part of the ionomer, both on entry and exit sides (even if they are more visible in the exit side).

These agglomerates were probably the result of the fast ionomer solidification process, which was probably speeded up by the cooling effect of water.
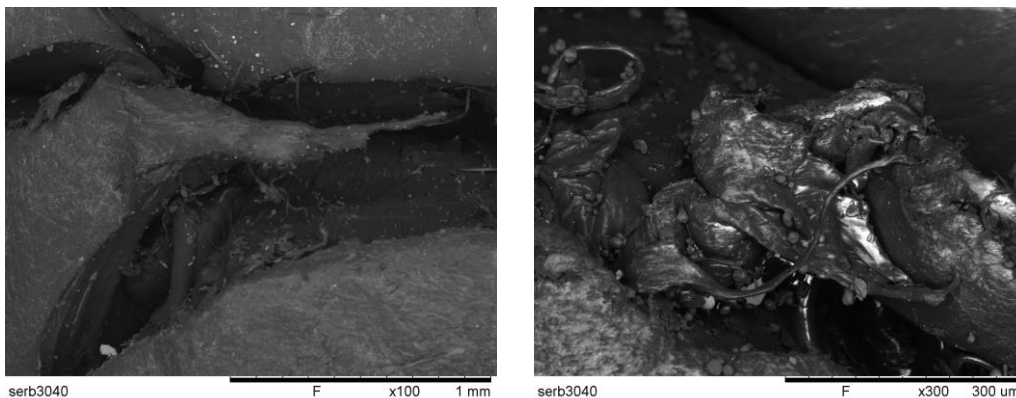
Figure 51 – SEM images for panel #302 (entry side)

(a) exit side x50

(b) exit side x150 of central core

(c) exit side x500,
upper-right branch of image b

(d) entry side
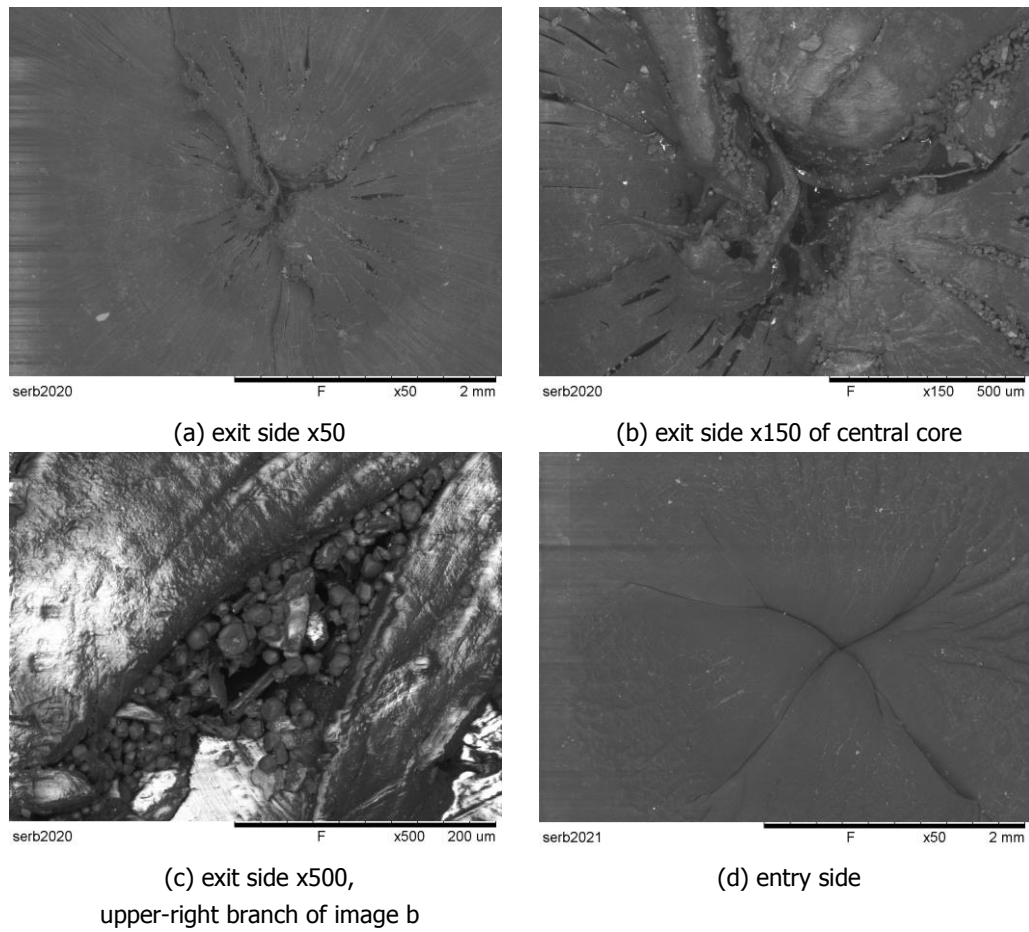
Figure 52 – SEM images for panel #202 (water, s=2mm, d=12mm, hole perfect closure)

3.2.3 Ballistic tests' discussion

3.2.3.1 S/d ratio healing analysis

Experimental tests showed an improved reparation performance in the case of water impinging the S8940 ionomer, especially with panel thickness of 2 and 3 mm with respect to the air environment condition, that is always taken as the reference case. However, in the case of the 1.5 mm panel, the healing performance was similar to the reference air environment one.

s \ d	5	6.34	8	10	12	14.3	16.6
1.5	0.30	0.24	0.19	0.15	0.13	0.11	0.09
2	0.40	0.32	0.25	0.20	0.17	0.14	0.12
3	0.60	0.47	0.38	0.30	0.25	0.21	0.18

Table 12 – s/d ratio healing table at 180 m/s in water environment

Table 12 can be transposed in Figure 53, and using the same concept adopted in the previous case, a green line and a red line could be represented, respectively linking the healing tested conditions and the non-repaired ones. The hypothetic frontier of healing is represented by the blue dashed line, obtained using a linear interpolation with the root mean square.

The change in healing response is underlined by the "knee" in the graph, showing a rapid increase in performance when the panel has a higher thickness.

Unfortunately, because of the experimental facility limitations, non-reparation confirmation was not possible to be checked in the case of 3mm-thick ionomer.
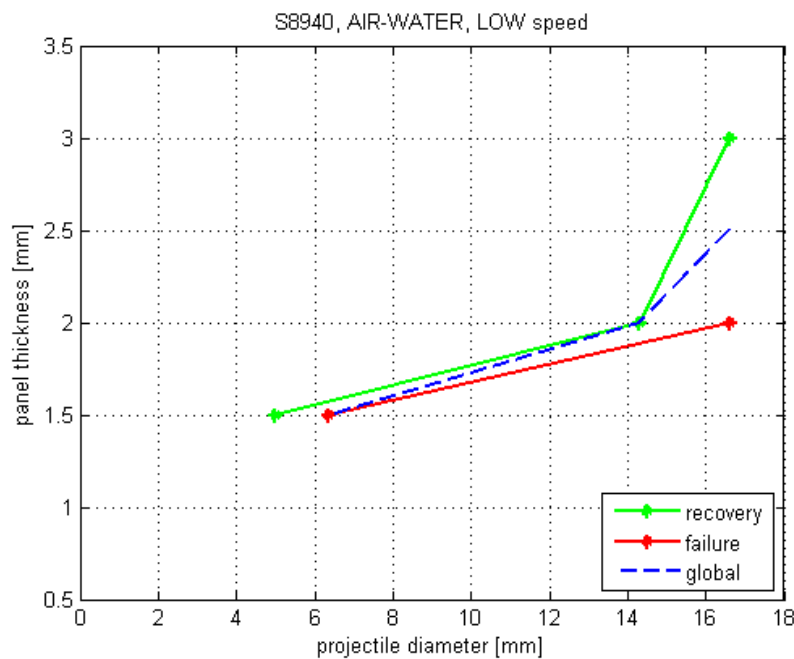
Figure 53 – s/d limit diagram in air-water environment

In order to explain the experimental results, some hypothesis have been formulated. Water was likely to have a positive cooling effect on the fused part of the ionomer and

to give a positive pressure sustainment on the panel deformation during the impact too.

The former idea consisted in the concept that water is able to cool more rapidly the fused part of the ionomer, due to its high thermal capacitance and because of its temperature of about 18°C (fusion temperature of the ionomer is about 96°C). Unfortunately, in the frame of the present thesis we were unable to capture the images in the infra-red band through a thermal imaging camera, as it was scheduled in the planning phase of this experimental campaign. In fact, during some precedent works ([23] [16]), some thermal imaging has been recorded, with findings that had always confirmed the reaching of the melting point of the ionomer, but with different values of maximum temperature. It will be of major interest to be able to retrieve some actualized data on impact and to compare those values with the water configuration case. Those results are a main candidate for the verification of the presented hypothesis on water cooling effect.

However, in support of the present considerations, pictures in §3.2.2.3 highlighted some grains that were never observed in air environment tests. Those agglomerates are supposed to be grains coming from a rapid solidification of the ionomer.

The latter hypothesis consisted in the idea that a liquid, with its pressure force on the backside of the panel, could reduce the deformation during the impact and perhaps increase the elastic return of the fused ionomer too. The ionomer is then supported in its return on its original non-deformed position, thus increasing the healing ability of the material. This idea is of far more difficult verification, and validation proposal of this hypothesis relies on a numerical modelling of the material behaviour in impact conditions (that for the moment is quite a far prospective).

3.2.3.2 Energy considerations

Energy considerations as described in the air case (§3.1.3.2) were not possible, since the presence of water implied a deceleration component that cannot be neglected as in the case of air. Mean velocity during the 10 to 15 cm after the impact is thus no more comparable with the instantaneous velocity value after the impact.

However, the ability of computing the mean velocity in a defined distance after the impact is preserved by the cylindrical Plexiglas configuration, but this value could only be an input to a numerical code able to retrieve the instantaneous velocity just after the perforation event.

An elementary numerical code was thus implemented in Matlab® in order to estimate the velocity profile inside the water. The main objective was to recover the instantaneous velocity value just after the perforation event starting from the mean velocity measurement (in fact, that velocity value would allow to perform considerations on the dissipated energy on the panel). However, because of tank architecture, also the first centimetres after the panel were in shadow. This fact generated a further complication.

The idea was to overcome this problem by observing the time lag between the impact with the panel and the appearance of the sphere inside the tube after the shadow lag. However, the run distance was small (40 mm) and the time lag very small too (a few frames at 21017 Hz). The probability of incurring in an experimental error was thus high, complicating the reliability of the code itself.

In addition, complexity of numerical model is augmented by the fact that Reynolds number for this phenomenon (around 10e5) fell in the cavitation zone. Evaluation of drag coefficient (C_D) was thus quite complicated.
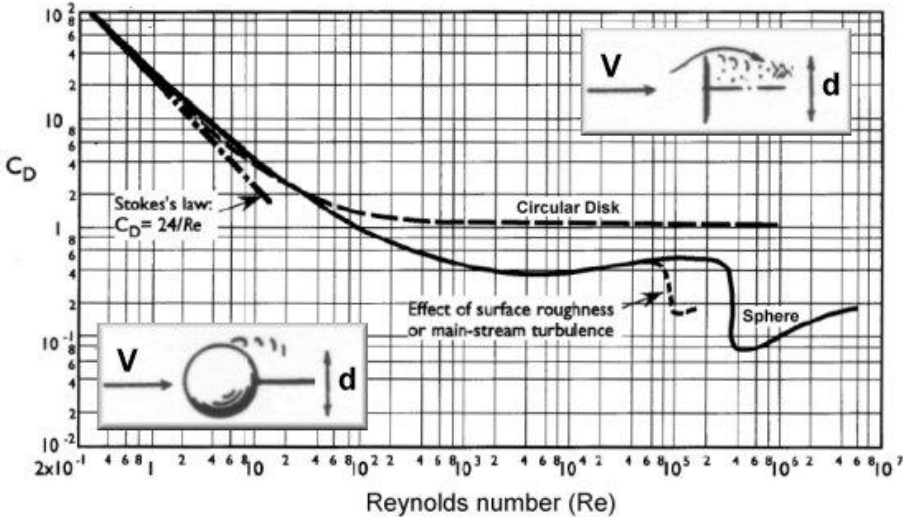
Figure 54 – Drag coefficient as a function of Reynolds number
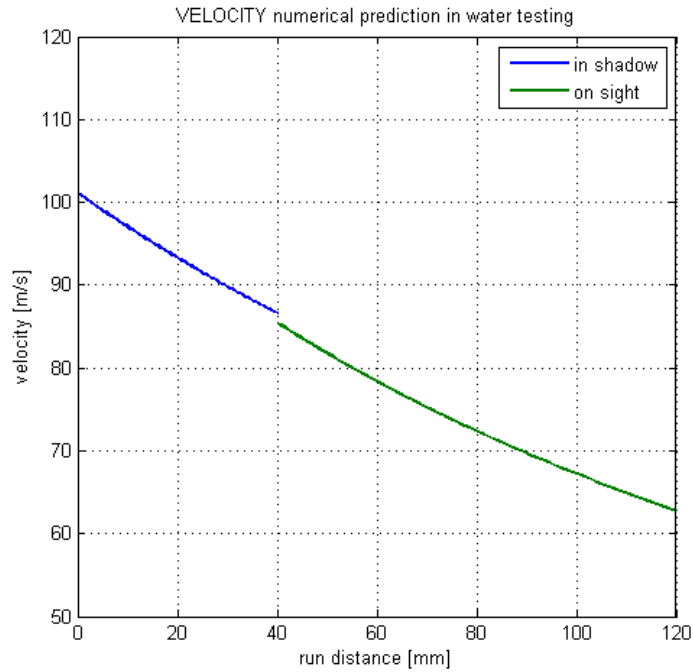
Figure 55 – Velocity prediction plot for panel 302.1

A total number of 10 tests were available, and some run of the code have been launched. The capability of providing a smooth plot in the discontinuity zone around the transition to the visible region (as in Figure 55) was a confirmation for a good code modelling, but these results were not replicable in a lot of circumstances.

Panel ID		Before Impact	SHADOW ZONE (AFTER THE IMPACT)				VISIBILITY ZONE (AFTER THE IMPACT)					Proj. Mass	s	Cd
		V_bfi [m/s]	v_in	d	Δ F	VM mis	VI calc	d	Δ F	VM mis	VF calc			
301	1	151.86										4.084	10	
302	1	189.15	101.05	40	9	93.41	85.84	80	23	73.10	62.27	4.084	10	0.4
302	2	110.62	72.25	50	15	70.06	61.40	80	32	52.54	45.12	4.084	10	0.4
201	1	236.44	error	40	4	210.17	112.75	90	20	97.00	79.32	4.084	10	0.4
201	2	186.82	136.35	50	8	131.36	129.05	70	12	122.60	116.64	4.084	10	0.15
201	3	189.15	error	50	6	175.14	98.25	80	20	84.07	72.22	4.084	10	0.4
202	1	161.67	error	45	8	118.22	95.00	50	12	87.57	80.91	7.057	12	0.4
303	1	152.04	error	45	12	82.24	55.6	60	25	50.44	45.85	7.057	12	0.4
303	2	148.87		45	7	135.11		40	10	84.07		11.868	14.3	0.4
203	1	116.76		45				0	0	0		7.057	12	0.4
203	2	176.39		45			111.85	45	9	105.09	99	11.868	14.3	0.4
304	1	181.51		45			117.7	105	21	105.09	93.94	18.74	16	0.4
204	1	182.76		45	5.5		122.6	90	17	111.27	101.05	18.74	16	0.4

Table 13 – Velocity profile computation in tank configuration.

Once having obtained the velocity after the impact, only a trivial operation of kinetic energy difference computation was necessary in order to compute the energy dissipated by the panel.

Only three cases were developed up to this stage, and results suggested a similar behaviour in terms of dissipated energy with respect to the panel in air environment. However, as evidenced in the code discussion, reliability of the code was quite low and the decision of abandoning the discussion was taken.

ID	V_{impact} [m/s]	$V_{residual}$ [m/s]	Mass [g]	A_{imp} (e-5) [m²]	E_{k_in} [J]	E_{k_fin} [J]	ΔE [J]	ΔE/A [J/mm²]	ΔE/V [J/mm³]	ΔE/m [J/kg]
302_1	189.15	101.05	4.087	7.85	73.11	20.87	52.25	0.57	0.22	12784
302_2	110.62	72.25	4.087	7.85	25.00	10.67	14.34	0.18	0.06	3509
207	186.82	136.35	4.087	7.85	71.32	37.99	33.33	0.42	0.21	8155

Table 14 – Dissipated energy computation table in air-water environment (partial results)

3.2.4 Pressure measurements

3.2.4.1 Experimental strategy overview

A total of seven tests have been done for the classical tank configuration with pressure sensors installed inside the cylindrical frame, but three of them have been discarded because the projectile was trapped inside the ionomer. The latter are reported and discussed in a later section because, in any case, they can be helpful for the description of the wave propagation inside the liquid.

The test setting for the four valid experiments is reported in Table 15. As it is possible to notice, all tests have been performed for 1.5 mm-thick panels only.

Panel ID	153	154	159	156
Explosafe	No	No	No	No
Projectile diameter [mm]	12	10	8	6.34
Panel thickness [mm]	1.5	1.5	1.5	1.5
Panel reparation	No	No	No	No
Transducer position	P3	P3	P3	P3
Sampling frequency	50 kHz	50 kHz	50 kHz	50 kHz
Signal cut frequency (F_c)	600 Hz	500 Hz	300 Hz	300 Hz

Table 15 – Test parameters for classical tank configuration

3.2.4.2 Signal critical analysis and filtering

Raw signal contained noise and thus the first operation that shall be done was to filter the sensors' output.

Some trials were performed in Matlab® software environment using the proprietary filter design tool (i.e. fdatool); the final selection fell on a Butterworth low pass filter with 40 poles. A group of cut frequencies (F_c) were tested and then the final was chosen specifically for every test by a graphical superposition compliance matching with the original signal.

In the present paragraph, the raw signals are represented in blue, while the filtered signals are plotted in red.

Generally, cut frequencies in the order of 2000 Hz still contained too much noise oscillations, while cut frequencies from 300 to 500 Hz had a good matching with the original signal.

However, the raw signal did not contain only noise, but also other disturbs that could be useful in order to drive some additional considerations.

Before proceeding to signal analysis, it is worth mentioning that in all pressure plots in the present thesis, the zero pressure value is the reference one, taken with the fluid at rest condition.
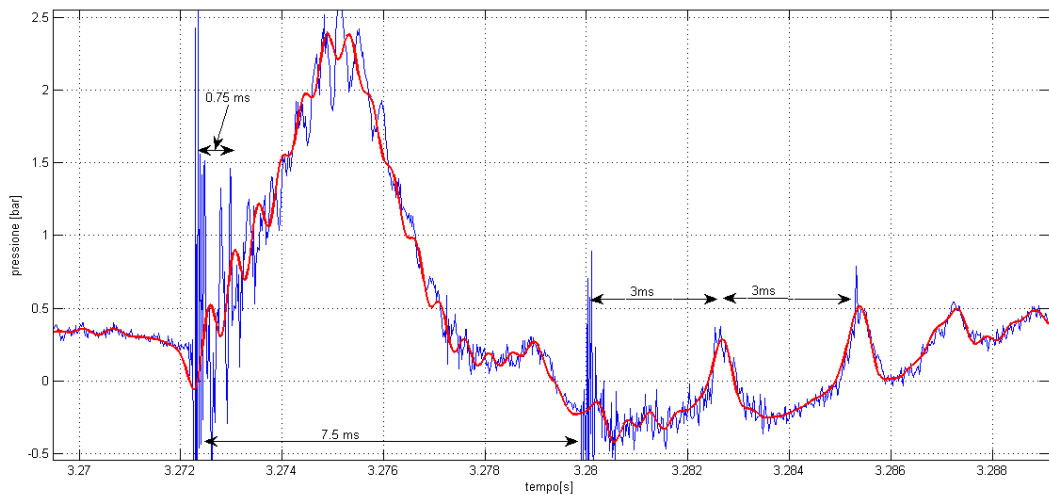
Figure 56 – Panel 154 raw pressure plot (in blue) and filtered signal (in red) at F_c=2200 Hz

In Figure 56, the first part of the pressure plot after the impact is represented. After a linear compression phase of around 30 milliseconds, a very high and instantaneous

distorted peak was observable. This was probably the footprint of the ionomer rupture event, when the projectile perforated the panel. Then, after the perforation, a compression wave was visible; in this point, the highest pressure peak is reached.

After the peak region, a number of oscillations of about 100 Hz frequency were sensed by the pressure gauge. Those were probably due to the interaction of the compression and expansion waves generated by the projectile impact and the passage of the bullet cavity region inside the tank.
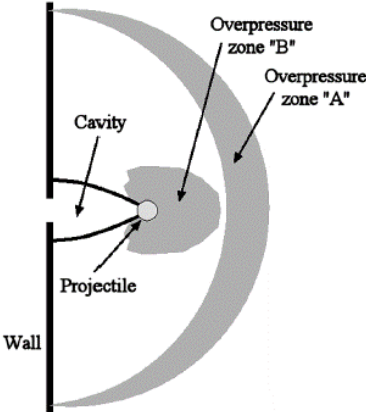
Figure 57 – Overpressure zones inside the fluid
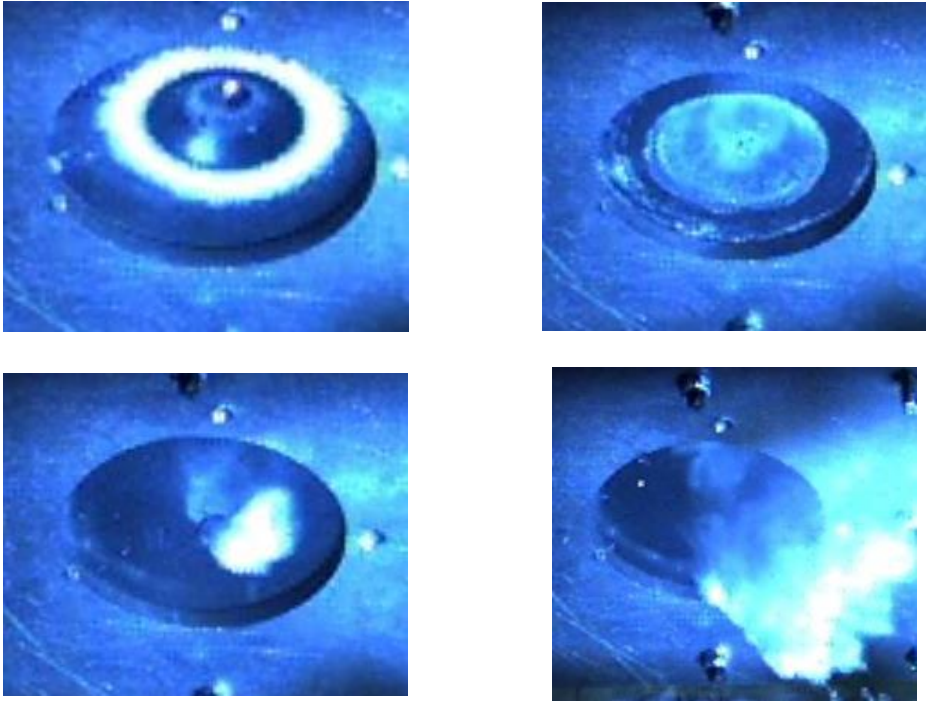
Figure 58 – Panel 153 frontal photos of impact

In fact, the following scenario was likely to happen inside the tank after the impact: the bullet penetrated the reservoir and a hemispherical shock wave was generated inside the liquid at the forefront of the projectile. This shock wave was the fastest wave inside the tank, followed by a classical compression-expansion wave and a sloshing wave. The first oscillations lasted for some milliseconds only, while the sloshing duration was in the order of some seconds.

The event just described is called hydrodynamic ram, and has been a field of research since many years [26] [27] [12].

Hydrodynamic ram's effects can be divided into three phases: the early shock phase, the later drag phase and the cavity phase.

The shock phase results from the energy transferred to the liquid as the projectile perforates the cell and impacts the fluid, creating a strong hemispherical shock wave centred at the point of impact.

In travelling through the liquid, the projectile loses energy to the fluid. This energy is transformed into kinetic energy of fluid motion. The projectile is also slowed by viscous drag.

The displacement of fluid during the drag stage forms a cavity behind the projectile. The subsequent expansion and collapse of the cavity are known as the cavitation stage. The oscillations of the cavity can cause significant pressure pulses. These pulses are less intense than the pressure generated by the shock wave, but have a longer duration in time.
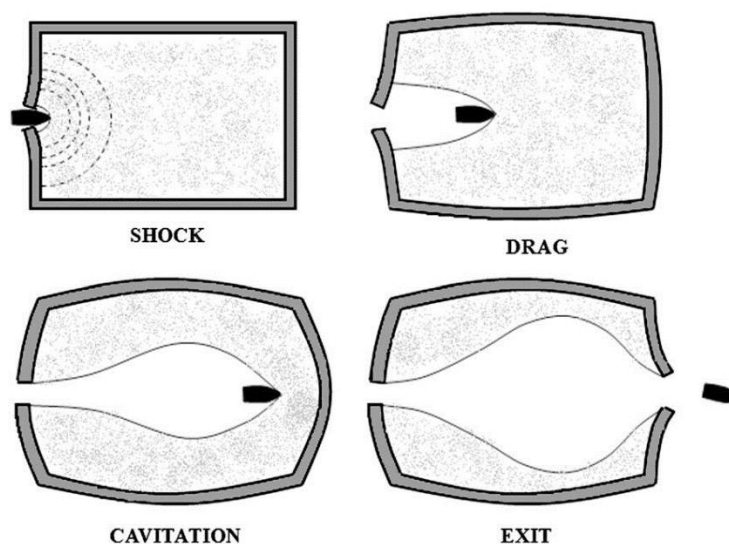
Figure 59 – Phases of hydrodynamic ram

Simulation of HRAM events has been attempted for over 30 years. The first methods employed to simulate HRAM were based on the use of the Piston Theory for the fluid–structure interaction. This theory assumes the normal reflection of pressure waves when reaching the walls of the structure, resulting in a one-dimensional response mechanism. The classical pressure theory failed to properly describe the effects of hydrodynamic ram, and an appropriate simulation code is needed in order to simulate the physical phenomenon. However, in the present thesis the interest is limited only to the description of the pressure wave that was experienced in the tank after the impact in different configurations.

In Figure 56, some peaks were visible in the original signals that probably did not belong to the just described HRAM phenomena. Those are the peaks located at 3.272 s and 3.280 s, and according to the most probable hypothesis that is going to be described, they are two projectile's impacts.
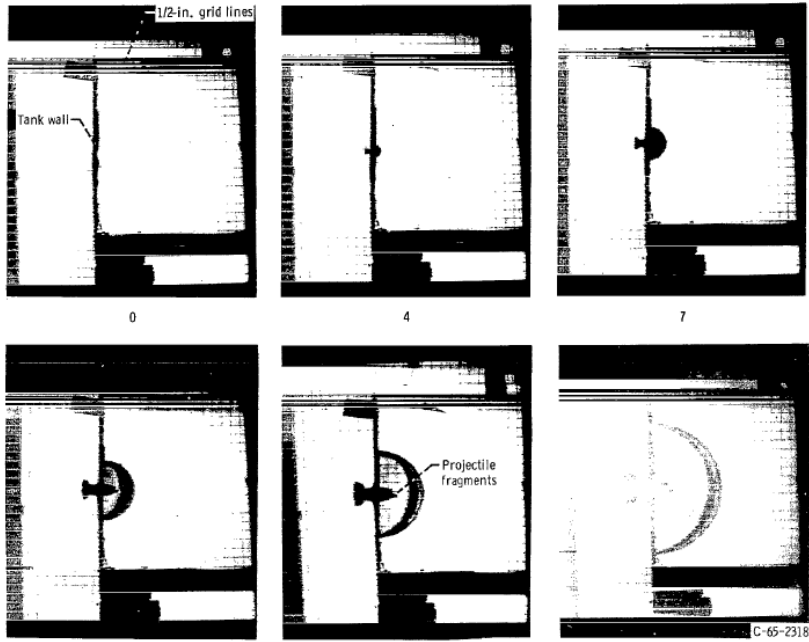
Figure 60 – shadowgraphs of pressure wave produced by impact in a water filled tank

From the high speed camera recordings done with the Plexiglas cylinder, there was evidence that the projectile experienced a fast velocity decay, expectable because of the drag component in the water is much larger than the one in air. This concept has been already discussed in §3.2.3.2. The developed and described numerical code was

run with the inputs coming from test number 154. The mean velocity for the whole run inside the tank was around 50 m/s. Considering the distance between the entrance wall and the back wall of 0.36 m, the time lag between the impacts would be about 7.2 milliseconds. It is a value very similar to the one evidenced in the graph (i.e. 7.5 ms). So, the peaks visible at 3.272 s and 3.280 s of the timeline could be the just described impacts. The peak at 3.285 seconds may be the final falling of the projectile on the bottom of the tank.

Peaks with distance of 7e-4 seconds could instead be due to the reflection of the initial shock wave between the tank walls. In fact, sound wave inside water at 20°C is about 1400 m/s, and the time lag to run the tank length in two directions is about 0.5 milliseconds ($0.72m/1484ms^{-1}$=5e-4s=0.5ms).
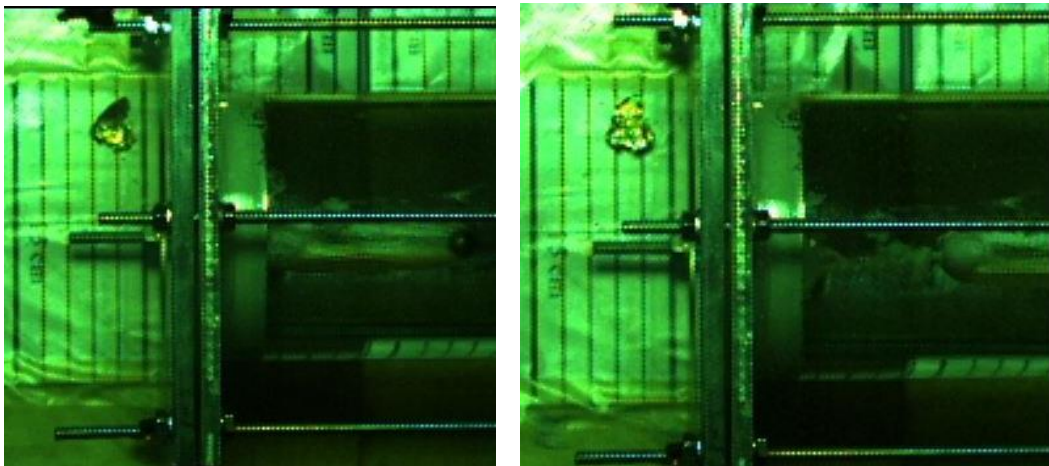
Figure 61 – Test 304 capture of projectile travelling inside water

3.2.4.3 Pressure filtered signals analysis and comparison

All the tests in Table 15 are hereby reported. It is possible to notice the phases described in the previous paragraph: initial compression, peak pressure, cavitation phenomenon and sloshing.

All the following figures represent only filtered value, since what described in the previous paragraph was accurately done for all the signals in order not to present a distorted filtered signal.
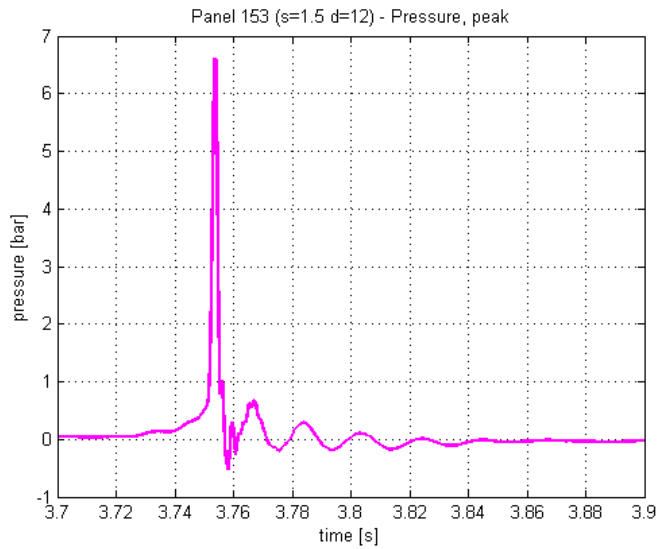
Figure 62 – Panel 153 pressure plot
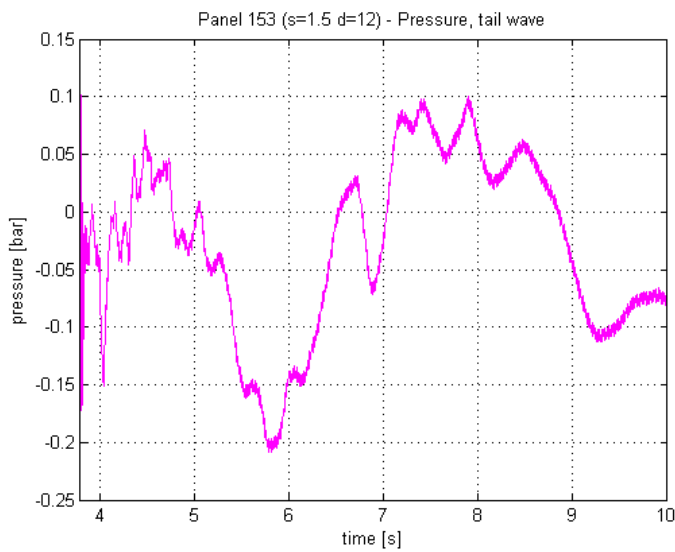
Figure 63 – Panel 153 pressure plot for the generated surface wave (sloshing)

The reference value – i.e. static pressure with calm fluid - is assumed at 0 bar.

Panel 153 pressure plot from sensor P3 (the same sensor was employed in all other tests reported in this paragraph) is represented in Figure 62 and Figure 63 in order to evidence the sloshing wave generated after the projectile passage into the tank tunnel. Sloshing, which was also visible from the camera, lasted for few seconds and had an

amplitude of some bar decimals only. On the contrary, the first phase after the impact was characterized by a higher amplitude and a few decimal of second.
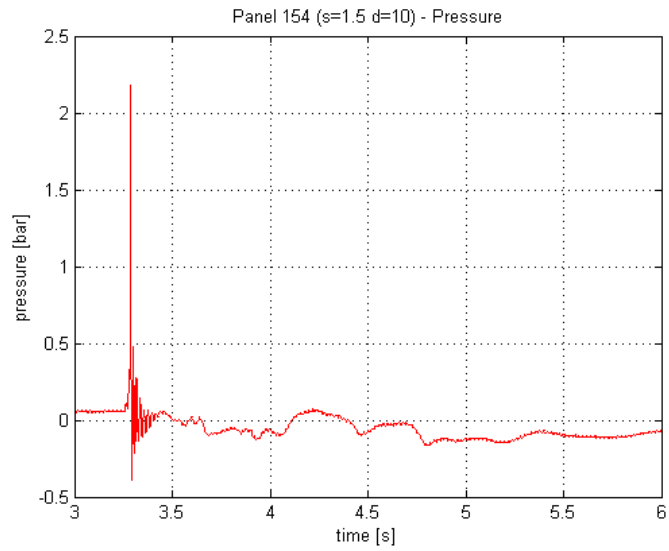
Figure 64 – Panel 154 pressure plot
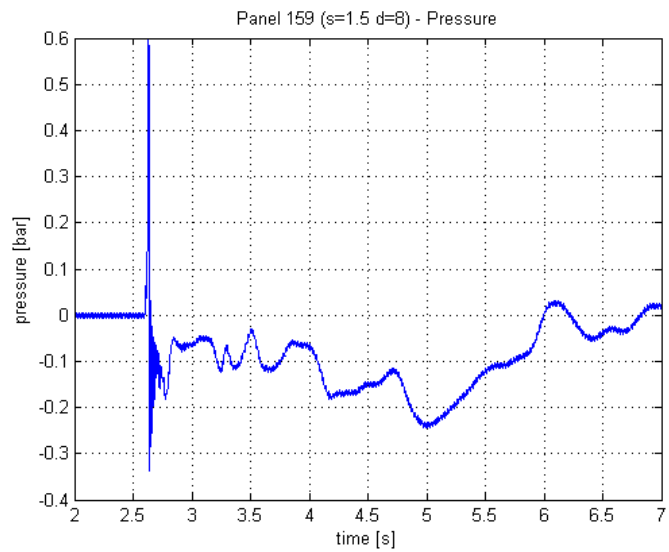
Figure 65 – Panel 159 pressure plot
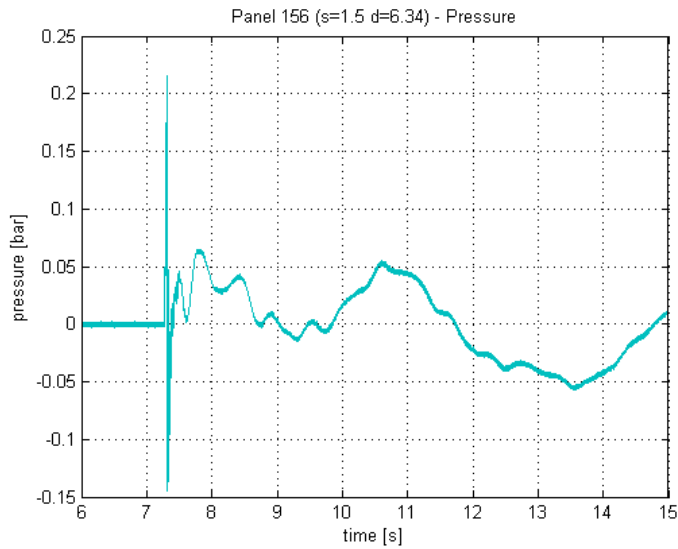
Figure 66 – Panel 156 pressure plot

As the projectile diameter increased, the peak pressure was higher, while there was no appreciable difference in the sloshing phenomenon: only a small decrease in the amplitude was registered with the sphere decrease, but the duration of the sloshing phase was similar in all the tests (i.e. from 5 to 10 seconds). The wave sloshing phase was also visible in some videos recorded with the Plexiglas cylinder: a wave ran back and forth until autonomously stopping.

Figure 67 and Table 16 were reported in order to give evidence to these results.

Panel ID	153	154	159	156
Projectile diameter [mm]	12	10	8	6.34
Peak pressure [bar]	6.7	2.2	0.59	0.22

Table 16 – peak pressure in tests with water (s=1.5 mm for all panels)
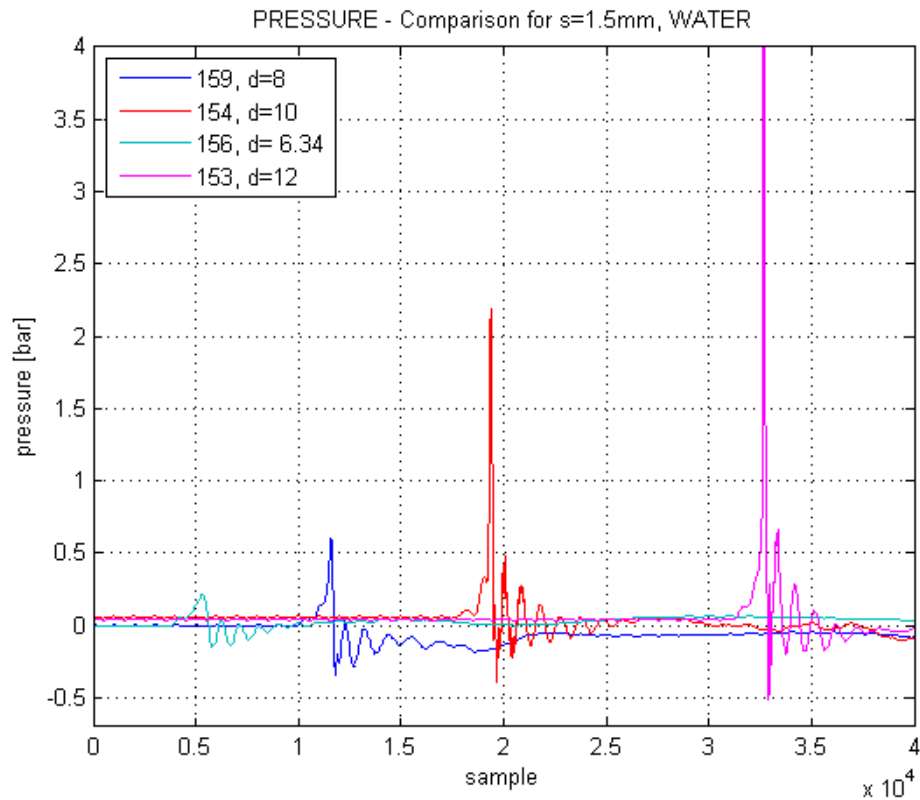
Figure 67 – Comparison graph for all tests in water with perforation of the panel
(for visualization purposes, signal 153 was cut in its maximum amplitude)

3.2.4.4 Wave study from the trapped projectile case

In order to complete the discussion of pressure waves inside the tank, it can be useful to analyze also the case in which the projectile was trapped inside the ionomer.
In fact, after this kind of impact, sensors were able to register a pressure wave without the effects generated by the projectile passage inside the liquid: no drag pressure and cavity wave were present inside the water, but only a compression-expansion wave.
From the video, it has been possible to extract the impact moment: the projectile (d=16.6 mm) hit the panel and a pressure wave along the ionomer itself was visible.
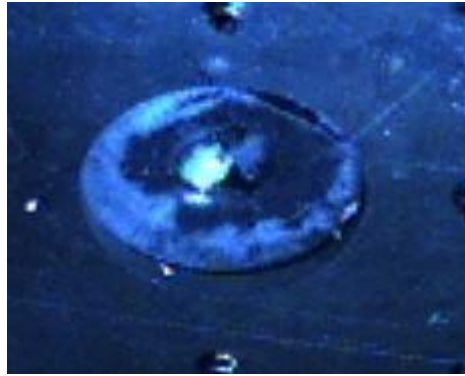
Figure 68 – Panel 310 frontal view of impact instant

The sensor positioned in P4 registered a pressure plot that resembled the ones already seen when perforation has happened. Clearly, as was expected, the value of the peak pressure was lower in this case (2.5 bar instead of around 10 bar for an equivalent case, even if with Explosafe). However, the pressure plot was composed of the same main phases: low compression, peak compression, compression-expansion phase, sloshing (even if it was strongly reduced).

Compression and expansion waves had a frequency of about 100 Hz and lasted for 50 milliseconds. If we suppose that two consecutive peaks are originated by the same wave, its velocity should be around 70 m/s. The sound velocity in water (at 20°C) is around 1400 m/s, and thus it should not be the case. Probably the wave is originated by the deformation of the panel itself that acts as a diaphragm or simply by the high energy impact on the panel (even without perforation).

In this case, with respect to the previously described cases, the signal was very smooth. The presence of the projectile inside the water and the consequent cavitation phenomena is likely to disrupt the signal, most of all in the first milliseconds. Also the generated wave (sloshing) is a characteristic feature found when the sphere perforated the panel.
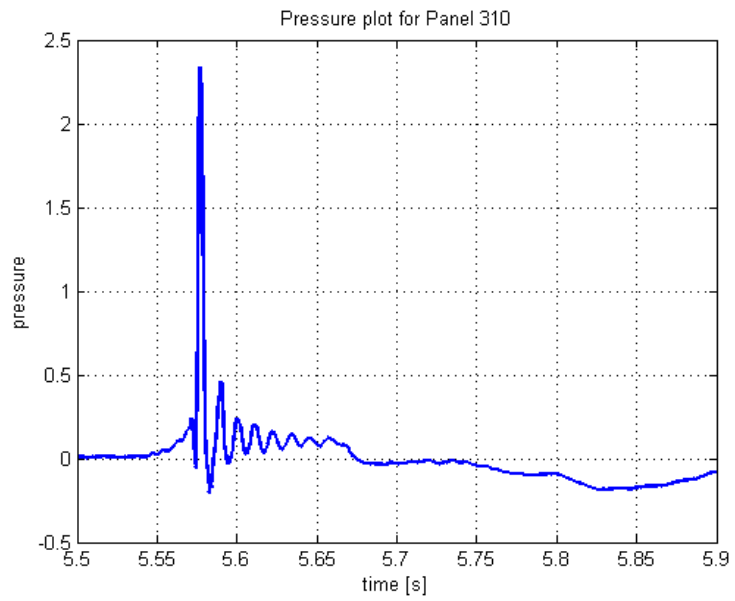
Figure 69 – Panel 310 (trapped projectile) pressure plot
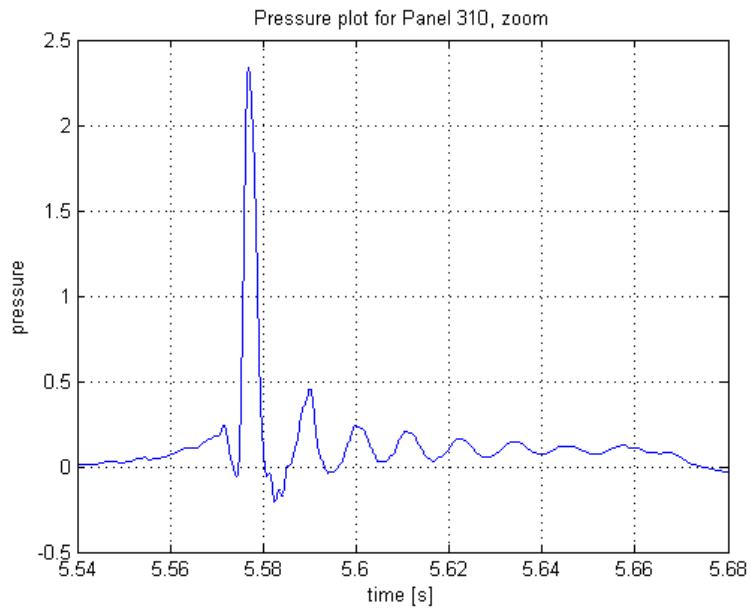
Figure 70 – Panel 310 pressure plot (zoom view)

3.3 Tests in air-water environment (tank) with Explosafe®

3.3.1 Experimental strategy and results' table

A total number of 13 ballistic tests have been performed with both the Plexiglas cylinder and the aluminium cylinder (Table 17), emulating the procedure adopted in the tank without Explosafe configuration. In the aluminium configuration it has been possible to record the pressure track during the impact phase through the pressure sensor (P3 or P4), while the Plexiglas architecture was aimed to observe the behaviour of Explosafe when subjected to the forces coming from the projectile.

Obviously, in tests with the aluminium cylinder, visibility inside the tunnel was precluded and no relevant information could be retrieved for both the sphere's velocity after the impact and the internal filler movement due to the projectile passage. However, even in the Plexiglas configuration no significant movement was recorded: the sphere's was totally concealed by the presence of the filler, and Explosafe itself did not show any movement. Consequently, any information on the projectile speed was lost. A positive aspect was certainly the response of the Explosafe in maintaining its integrity. However, the high speed camera position was no more of particular value: the only information that was able to record was the velocity before the impact, as in the previous tests with the total aluminium tank. That velocity is yet quite constant if the cannon settings are well controlled, as it is confirmed by about the first half of the tests in the present thesis and was studied in previous thesis [insert L.Nov. reference]. Consequently, the decision of changing the position of the camera was taken, in order to record the ballistic impact event on the panel surface. In fact, no frontal video was available before, since the priority was always given to the possibility to record the velocities before and after the impact.

3.3.2 Healing morphological analysis

3.3.2.1 Visual

As before, the first operation was a visual analysis of the impact region at naked eye. Repaired panels presented a morphological similarity to the self-healed ionomers during water tests. The presence of water reduced the *petalling* tendency of the fused part, giving a more axial-symmetric shape to the healed region. An example is reported in Figure 71.
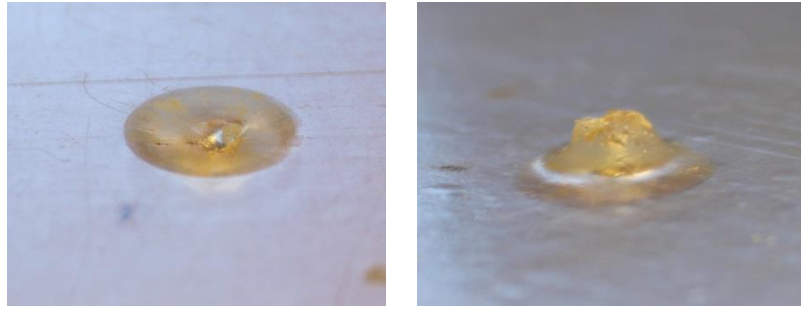
Figure 71 – Panel 311 entry and exit side respectively

The non-repaired ionomers were characterized by a formation of a single petal on the exit side, as evidenced in panels 309, 210 and 307 (Figure 73). In most of the cases, the petal had a rounded shape, and it remained slightly lifted form the panel.

Panel 208 was, instead, the worst repaired case ever seen in all tests until now. A complete portion of the ionomer was ejected and reparation completely failed.

A concentric morphological region division was present also in these panels. The inner region of the impact area was characterized by petals or an axial-symmetric protruding solidified fuse, while an outer region, whose diameter is delimited by the sphere's diameter, presented a bulking region but no cracks on its surface.

Figure 72 – Frontal view of impacted panel mounted on the tank yet

By visual inspection of the panel before removing it from the tank, it was possible to notice the traces of the projectile passage: Explosafe did not experience a high deformation, but a cavity was visible just behind the impact area.
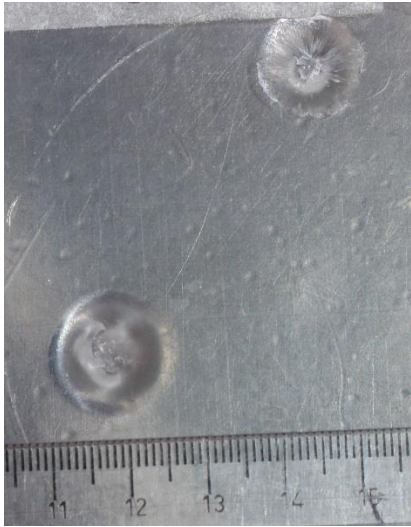
Panel 309 – entry side
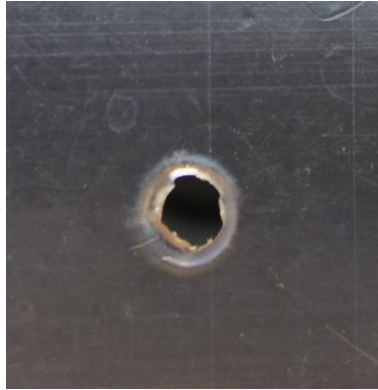
Panel 208

309 – exit side

210 – exit side
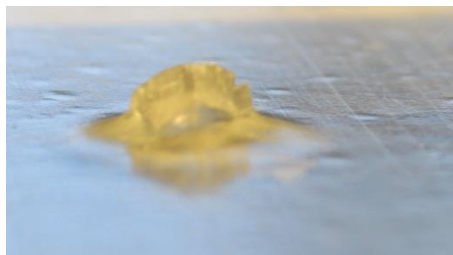
307 – exit side

Figure 73 – Photographs of impact region on panels tested with Explosafe inside the tank

3.3.2.2 Leakage tests

Panel ID	s [mm]	d [mm]	s/d	WATER leakage	AIR leakage	RESIDUAL HOLE < 1mm
210	2	12	0.17	True	True	False
309	3	14.3	0.21	False	True	False
158	1.5	8	0.19	True	True	False
208	2	14.3	0.14	True	True	True
209	2	12	0.17	True	True	True
307	2	14.3	0.14	False	True	True
309	3	16.6	0.18	True	True	True
211	2	10	0.20	True	True	True
213	2	8	0.25	True	True	True
155	1.5	6.34	0.24	True	True	True
311	3	10	0.30	False	False	False
212	2	8	0.25	False	False	False
160	1.5	6.34	0.24	False	False	False

Table 17 – Tests in Explosafe configuration and leakage results

The first observation of spillage has been performed with the panel still on the tank. Events in which the water spillage was present were in a larger number than in tests without Explosafe, due to a wider residual hole diameter.
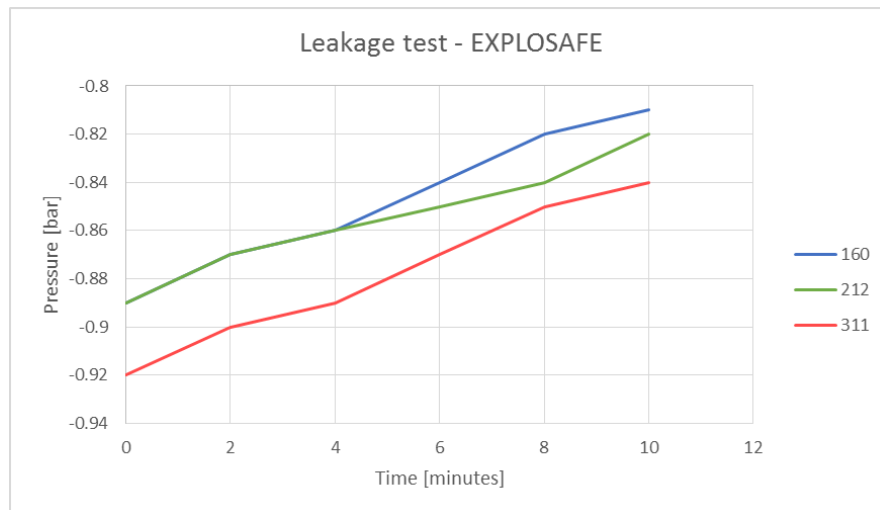
Figure 74 – Leakage tests graphs on repaired panels (water-Explosafe environment)

3.3.2.3 SEM

Analysis at the microscope for Panel 311 showed the petals' division in blocks. It seemed that a precise cut was done, instead of a not perfectly linear crack as visible in previous testing configurations. The idea that Explosafe aluminium cells can operate this cut during the physical contact with the ionomer in the deformation phase could be confirmed by the acquired images.

Groups of filaments were clearly visible too, suggesting that the presence of water could accelerate the cooling phase of the external part of the ionomer and thus leaving a more discontinuous surface.
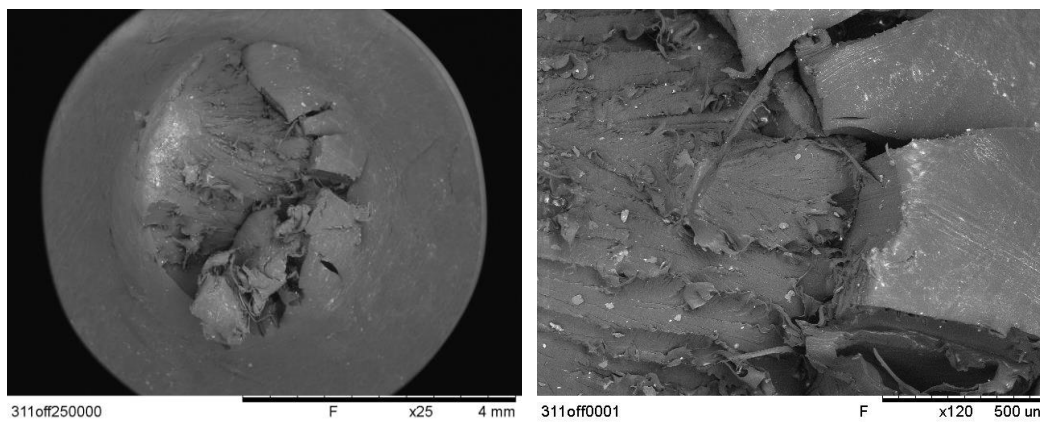
Figure 75 – Panel 311, exit side

Panel 160 showed a particular sealing region on the entry side. In other configurations, a sort of continuous line at the petals conjunction was visible. In this case, on the contrary, the sealing shows more continuity in some regions but also the presence of filaments in others.
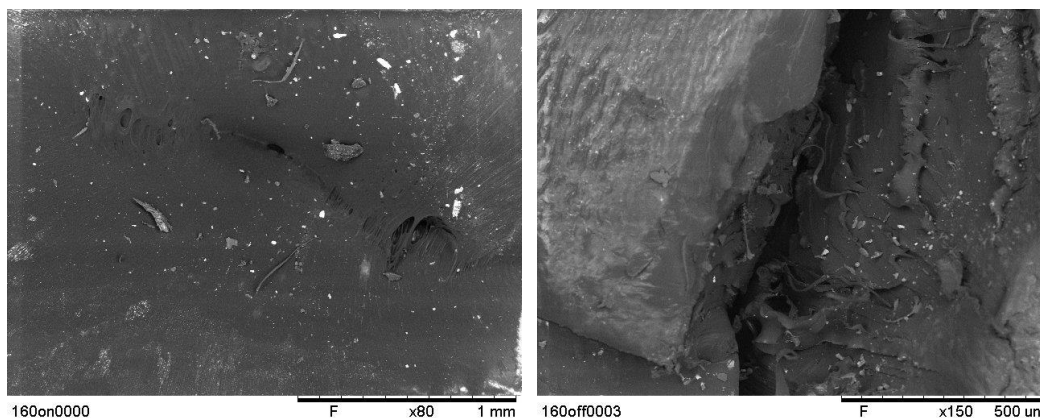
Figure 76 – Panel 160, entry and exit sides

3.3.3 Ballistic tests' discussion

3.3.3.1 S/d ratio healing analysis

Conducted tests showed a decrease in reparation performance not only with respect to the water configuration, but also with respect to the air reference case. Critical s/d ratio is between 0.25 and 0.21, a much higher ratio than the promising 0.12 experienced in the water case tests.

Moreover, the 3mm-thick panel showed a reparation in all tests when ratio was higher than 0.21, but that was not the case for smaller thickness panels, in which there was a probability of 50% of reparation even for large characteristic ratios.

s \ d	6.34	8	10	12	14.3	16.6
1.5	0.24	0.19	0.15	0.13	0.11	0.09
2	0.32	0.25	0.20	0.17	0.14	0.12
3	0.47	0.38	0.30	0.25	0.21	0.18

Table 18 – s/d ratio healing table at 180 m/s in water environment, with Explosafe®

The just proven capability of water was then totally cancelled.

This negative effect could be due to the mechanical interaction between the panels and the internal filler, which increased the shock wave intensity in proximity of the wet side of the panel.

A further possible reason could be the physical cut of the molten ionomer portion during impact deformation, when it came in contact with the sharp hexagonal cells of the aluminium filler.

This second hypothesis could be supported by visual and SEM analysis, while the higher shock intensity reason could be sustained by some frames extracted from the high speed camera videos or by installation of pressure sensors inside the tank.

In §3.2.4, it is possible to see that a slight increase in the pressure peak just after the impact has been measured.

Frames of the impact captured at 21017 Hz (or more) with the high speed camera, showed a reduction of the wave reflection intensity from the sides of the cylinders, but also a more consistent white wave in the proximity of the impact region. It seemed that a part of the wave was reflected by the near aluminium filler, while the part of the wave that extended towards the sides was weakened and its reflection was not as intense as in the case without Explosafe.

The possibility to install a pressure gauge in the proximity of the ionomer panel has been postponed because of limitations on available sensors (actual range was 10 bar).
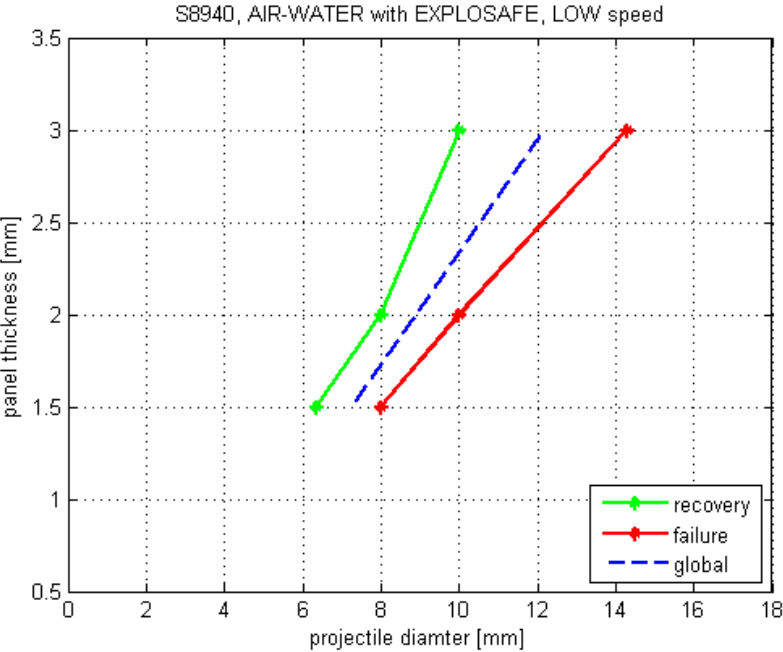

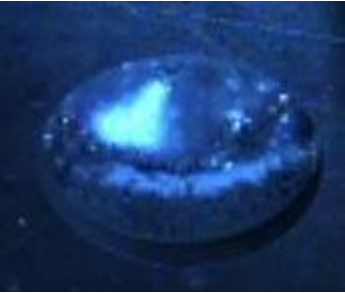Figure 77 – s/d limit graph construction for ionomer in contact with water

Figure 78 – Panel 309 wave after impact detail

Figure 79 – Panel 211 impact frames from high speed camera

3.3.3.2 Energy considerations

Because of the internal filler presence, it was not possible to recover the internal spheres velocity in a visual way. In fact, visibility was totally precluded and the filler did not experience a visible motion: even during the impact it did not show any kind of deformation from an external viewer.

However, in some cases, it was possible to recover the measures of the probable time lag between the ionomer's perforation and the impact with the back plate of the tank by using the raw signal from pressure gauges.

Following a similar procedure to what performed in §3.2.4.2, it was possible to compute the mean velocity of the projectile inside the tank, and from that, through the numerical code, recover the velocity profile.

In fact, the initial velocity inside the tube is a core element in order to compute the dissipated energy.

It was quite unexpected to find higher velocities with respect to its twin case in water environment (§3.3.4.2).

Even if it would be necessary to gather some more data, the following hypothetical explication could be done:

- The projectile reached the panel with the same speed as in its case with only water inside;

- The ionomer panel did break some instants before than the water case. The driving idea was that both a high shock wave constrained on the entry panel backside by the Explosafe presence and the cutting effect of the aluminium foil made the ionomer break before than the other case, decelerating the sphere a bit less.

- The aluminium filler placed inside the tank was a physical obstacle. We were expecting thus the mean velocity to be smaller. However, Explosafe was likely to act as a decelerating obstacle, but what we are suggesting is that the initial velocity inside the tank could be higher enough to compensate also this decelerating component.

- The mean velocity was then a little bit higher in the twin case with water, as revealed by the pressure sensor oscillations.

3.3.4 Pressure measurements

3.3.4.1 Experimental strategy and available tests

A total number of eight tests have been carried out with pressure transducers mounted either in P3 or in P4 position (Figure 34) in the tank configuration with cylindrical Explosafe.

Differently from the simple tank case, in this configuration also the panel thickness has been changed.

However, only six tests were considered valid for the pressure analysis. They are reported in Table 19.

Panel ID	309	311	211	213	158_1	155
Explosafe	Yes	Yes	Yes	Yes	Yes	Yes
Projectile diameter [mm]	16.6	10	10	8	8	6.34
Panel thickness [mm]	3	3	2	2	1.5	1.5
Panel reparation	No	Yes	No	No	No	No
Transducer position	P4	P3	P3	P3	P3	P3
Sampling frequency	21 kHz	50 kHz	50 kHz	50 kHz	50 kHz	50 kHz
Signal cut frequency (F_c)	600 Hz	300 Hz	600 Hz	300 Hz	200 Hz	300 Hz

Table 19 – test parameters review table for Explosafe tank configuration

3.3.4.2 Pressure transducer signal critical analysis

Considerations already described in §3.2.4.2 are still valid in this section: the same trial and error filtering procedure was adopted in order to select the apparently best cut frequency that was able to describe the water pressure variations after the impact.

In general, a filtering frequency with values ranging from 200 to 600 Hz was adopted in all analysed cases.

The compression and expansion phases found in the water case are clearly visible in this case too: a first smooth compression phase, followed by the peak pressure made of only one short compression and some smaller compression and expansion waves. In the whole set of proof, sloshing was not visible but for one second in the worst case.
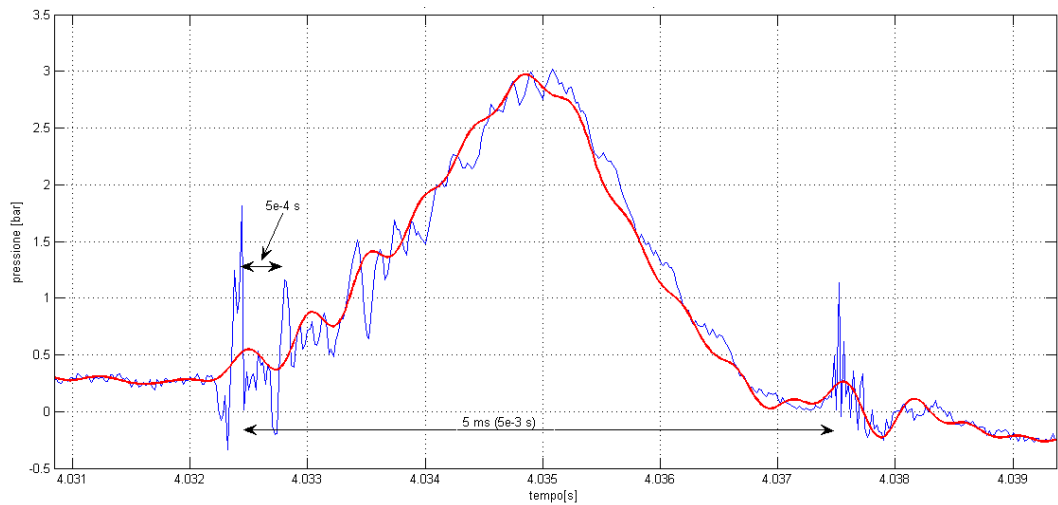
Figure 80 – Panel 211 pressure plot, with cut frequency (in red) at 2200Hz

In some pressure plots, as in Figure 80 and Figure 81, short and high peaks were visible in the vicinity of the perforation instant and after some milliseconds. The same concept explained in the already mentioned paragraph is considered for the explanation of that disturbance: they could represent the ionomer perforation instant and the bullet impact on the back plate of the tank. Numerical computations have been carried out by using both the mean velocity from the pressure gauges signals and the simple numerical code developed in §3.2.3.2 .
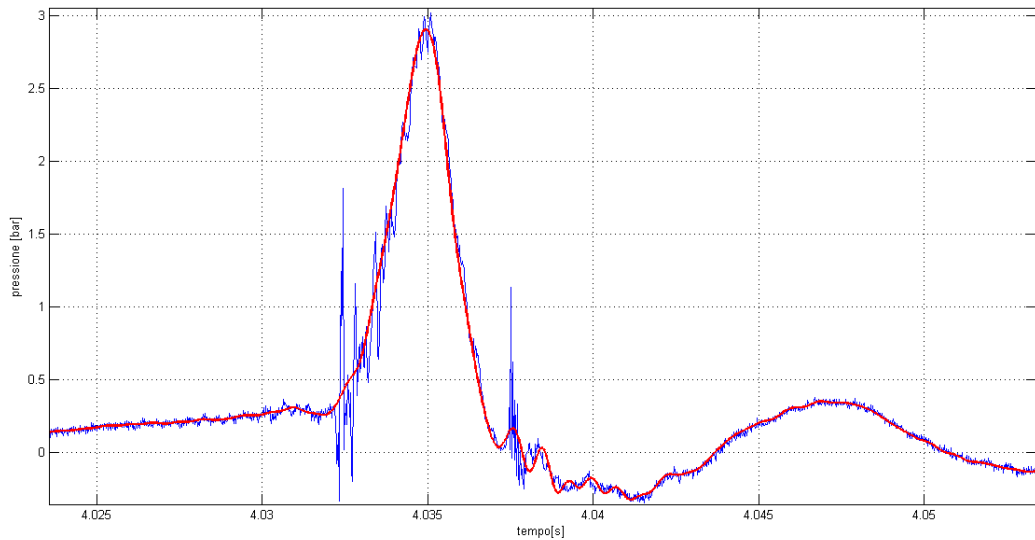

Figure 81 – Panel 211 pressure plot, with cut frequency (in red) at 600 Hz

Considering the tube length of 0.36m and the time lag of 0.005s from the first peak (at t=4.0325 of the recording) to the second one (at t=4.075s), the mean velocity along the tank was about 72 m/s. The track inside the tube was affected by a deceleration that cannot be neglected. However, despite the previous case in which the deceleration was driven by the water drag, in this case it was due to a new configuration: water and the filler. In this case, there is no data about the correct drag coefficient for water, neither a known way of modelling the presence of the filler. The decision to use the same drag coefficient of the water case was taken, unless the results would suffer of low reliability concerns.

The initial velocity after the impact is computed to be 155 m/s, while the final velocity before the impact against the back plate of the tank is estimated to be 39 m/s. This velocity set satisfies the mean velocity requirement of 72 m/s, considering C_d=0.4.

The lack of the "third" peak is justified by the fact that the projectile is entrapped inside the aluminium filler, and did not hit the lower part of the tank when all its velocity has been lost.

Contrary on the expectations, in the case of water without Explosafe, the projectile mean velocity along the tube was about 50 m/s. This mismatch is hardly explicable, since Explosafe should have increased the sphere's deceleration by creating a barrier to the projectile movement. As already mentioned, a possible motivation relied on the fact that Explosafe could anticipate the ionomer rupture by physically cutting the deformed part ahead of the sphere. However, further investigations should be done in order to validate this hypothesis, perhaps also adding some acceleration sensors on the tank frame.

3.3.4.3 Pressure filtered signals

In the present paragraph, pressure plots for all tests available with Explosafe are reported.

The time axis does not start always at the same instant because of the difference in the trigger action, but the interest is on the duration of the pressure wave. In fact, differently from the traditional water case, only the phases of constant pressure increase, peak pressure (only some milliseconds long in time) and compression/expansion wave is present. Sloshing, which was the longest event, is quite completely cancelled by the presence of Explosafe.
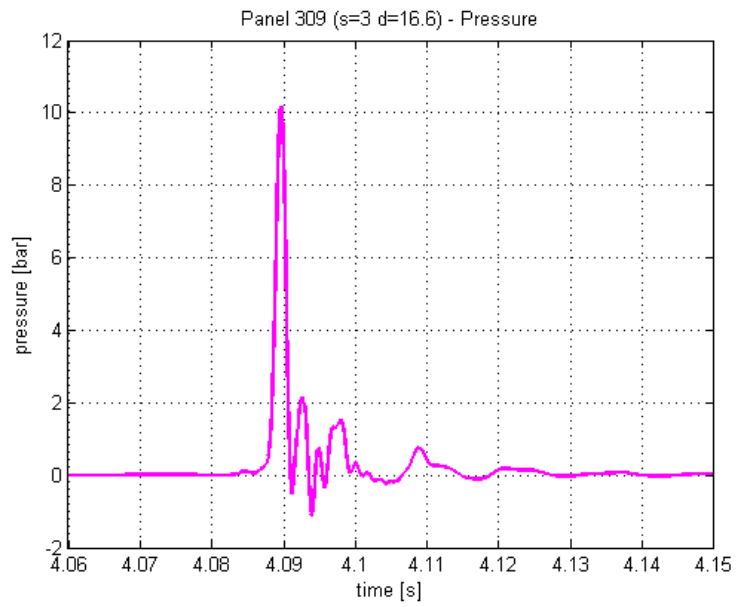
Figure 82 – Panel 309 pressure plot
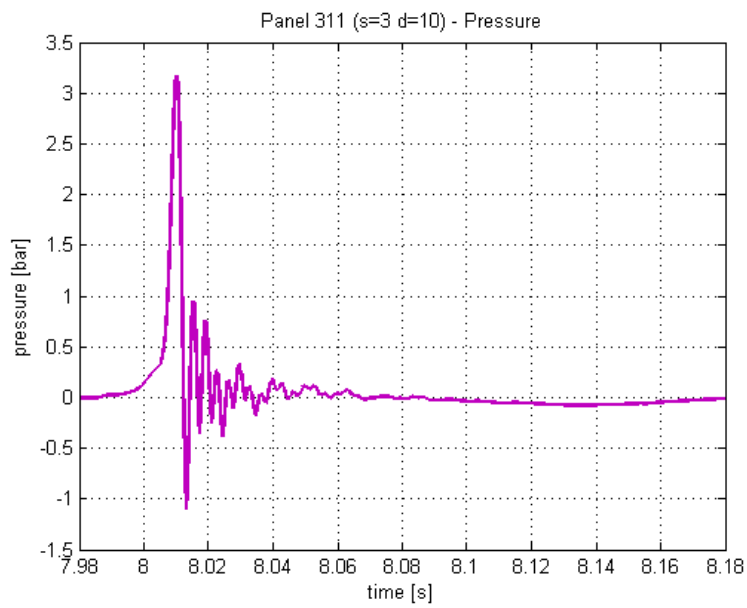
Figure 83 – Panel 311 pressure plot
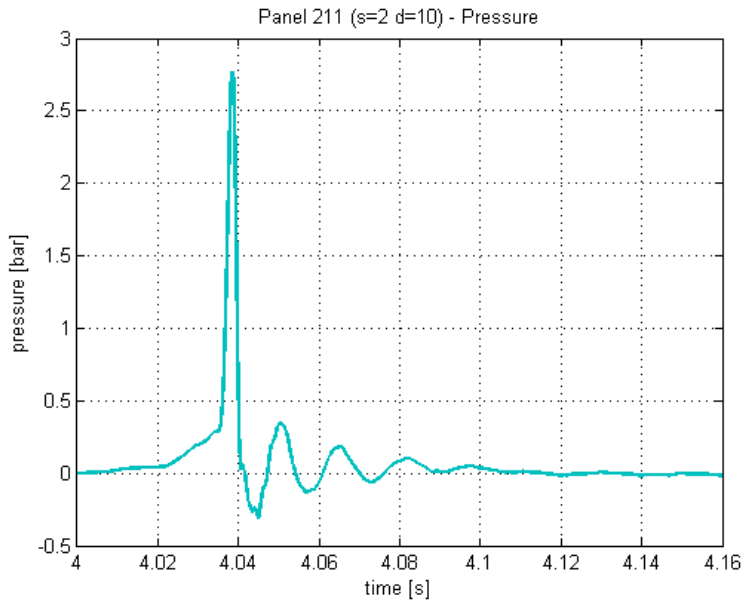
Figure 84 – Panel 211 pressure plot

Another observation that is worth to mention is referred to test done with the 8 mm diameter sphere. As it is possible to see in the pressure plots for panels 213 and 158, the shape is very different from all other cases, and also the intensity of the peak pressure is strongly reduced. The motivation should be a particular interaction between the 8 mm diameter sphere and the aluminium matrix of Explosafe.
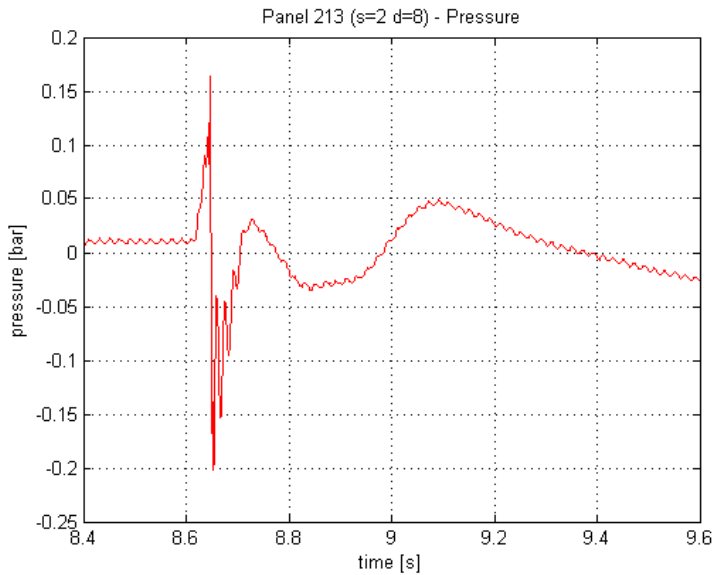
Figure 85 – Panel 213 pressure plot
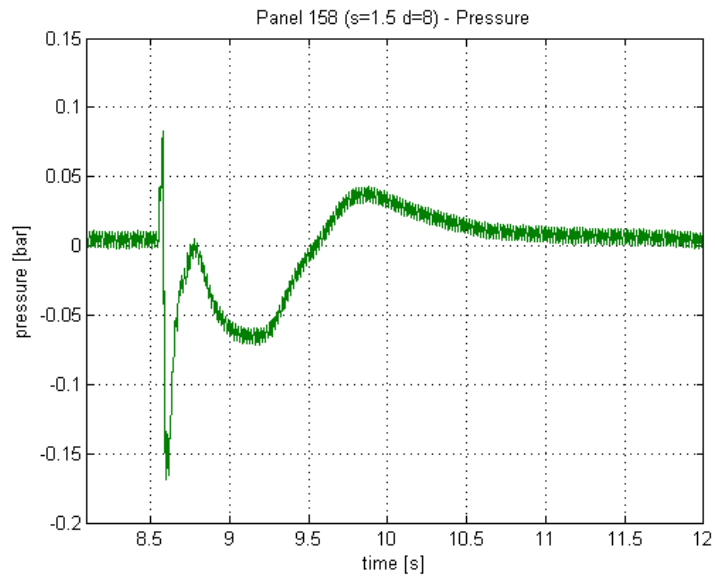
Figure 86 – Panel 158 pressure plot

In the case of diameter 6.34 mm, the pressure wave shape resembled all the other cases, and not the particular one that was put in evidence in Figure 85 and Figure 86.
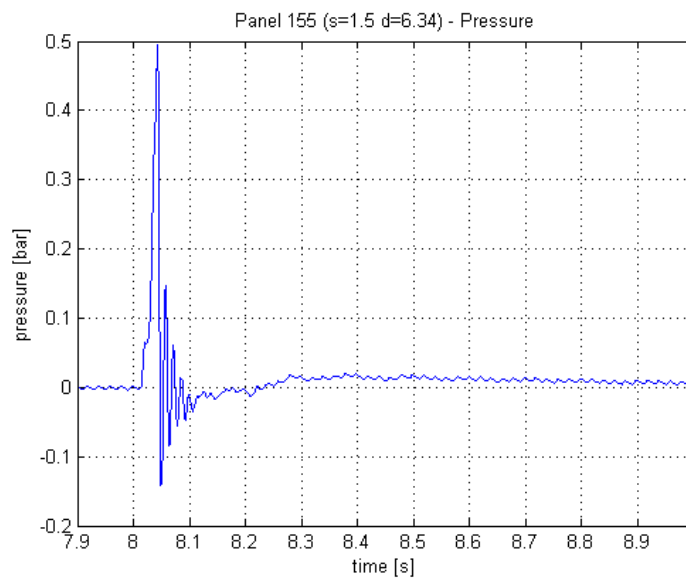
Figure 87 – Panel 155 pressure plot

3.3.4.4 First comparison of homologue case with and without Explosafe

In order to reach a better understanding of the peculiar characteristics of Explosafe under ballistic impacts, in the next paragraphs the signal is compared with the homologues cases without the internal filler.

The first comparison set is described in Table 20.

Panel ID	158_1	159
Explosafe	Yes	No
Projectile diameter [mm]	8	8
Panel thickness [mm]	1.5	1.5
Panel reparation	No	No
Transducer position	P3	P3
Sampling frequency	50 kHz	50 kHz
Filtering	200 Hz	200 Hz

Table 20 – Pressure comparison set for d=8 mm and s=1.5 mm

From Figure 88 it was possible to conclude that there was a sensible attenuation of the pressure variations in the long time frame: the variations that are supposed to be the representation of the surface waves are now totally absent. Within one second only from the high energy impact event, the water was calm. This was not the case for the water tests, as it is highlighted in blue: pressure variations lasted for some seconds and had a moderate intensity. In other words, Explosafe consistently reduced sloshing.
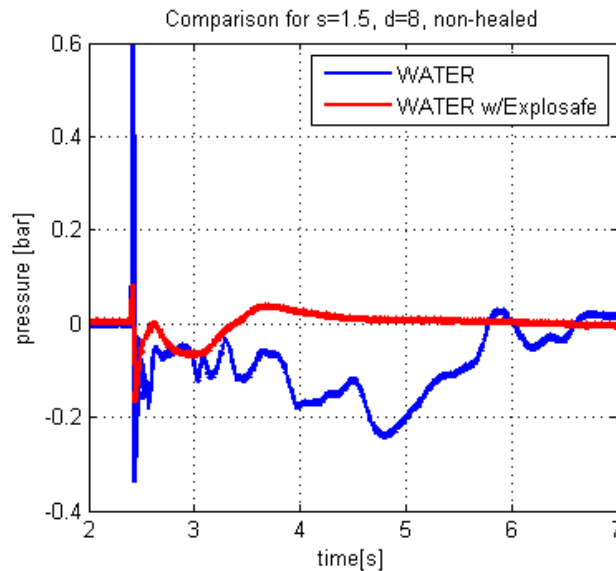
Figure 88 – Pressure plot (long time lag)
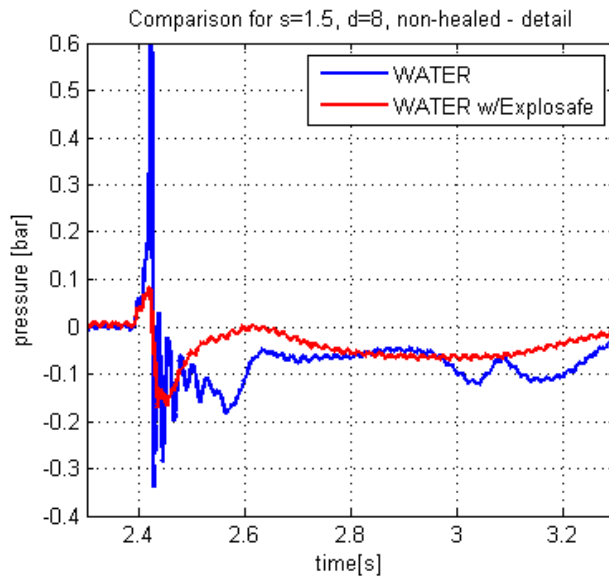
Figure 89 – Pressure plot (medium time lag)

Figure 89 and Figure 90 focus the attention on the first decimals and centesimal of seconds after the impact.

In this test, Explosafe reduced the peak pressure and provided a strong attenuation to the high frequency pressure variations just after the impact.

Globally, in this test, Explosafe demonstrated the capability of attenuation of the entire set of dangerous effects of projectile penetration inside a tank: initial peak pressure, high frequency oscillations and sloshing for some seconds after the impact.
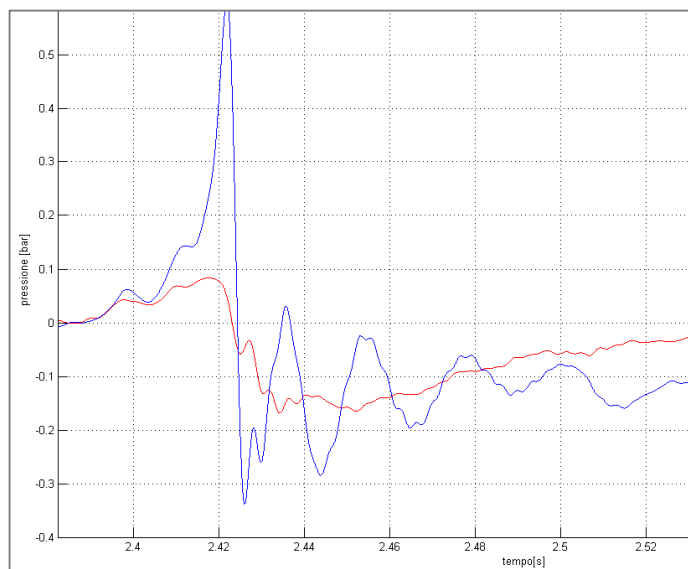
Figure 90 – Pressure variations comparison in the first instants (blue: water; red: with Explosafe)

3.3.4.5 Second comparison of homologue cases with and w/o ES

In this paragraph, the compared set is different from the previous one in the projectile diameter only.

Panel ID	155	156
Explosafe	Yes	No
Projectile diameter [mm]	6.34	6.34
Panel thickness [mm]	1.5	1.5
Panel reparation	No	No
Transducer position	P3	P3
Sampling frequency	50 kHz	50 kHz
Filtering	300 Hz	300 Hz

Figure 91 - Pressure comparison set for d=6.34 mm and s=1.5 mm

Sloshing cancellation is visible from Figure 92, giving confirmation to the already observed results.

However, in this case, the peak pressure for the case with Explosafe was higher than its twin set without the internal filler, and the high frequency oscillations were not cancelled too.
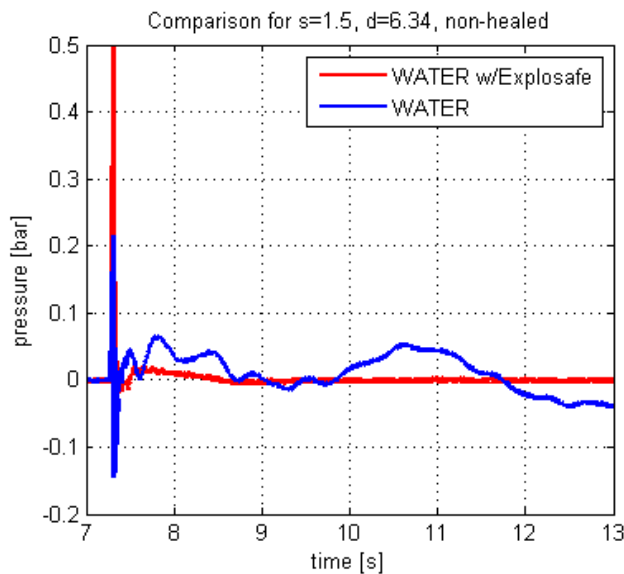
Figure 92 – Pressure plot for long time lag

The possible motivation to the increase in the peak pressure could be because it was the resultant of two components: one due to the impact and the penetration of the sphere inside the water tube, and the second due to the compression given by the filler

deformation itself. In fact, Explosafe could work as a sort of piston in compression phase, thus adding a pressure component to the initial compression phase.

The filler deformation could be due either to friction with the sphere or to the panel deformation that pushed the part in contact with Explosafe or by a combination of both.
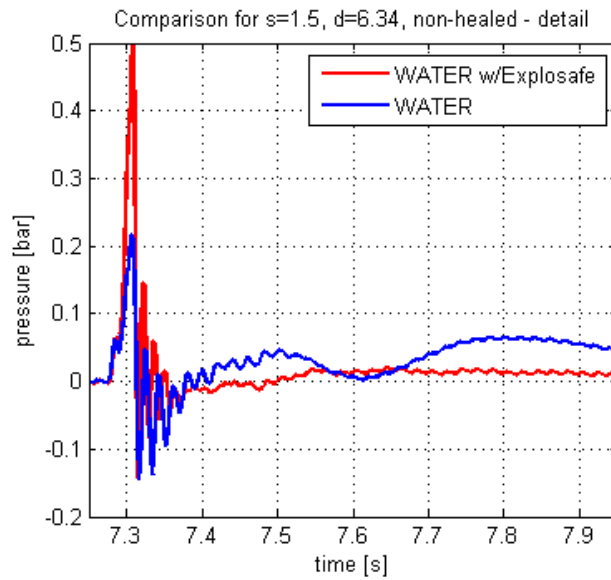
Figure 93 – Pressure plot for the first decimals of second after the impact
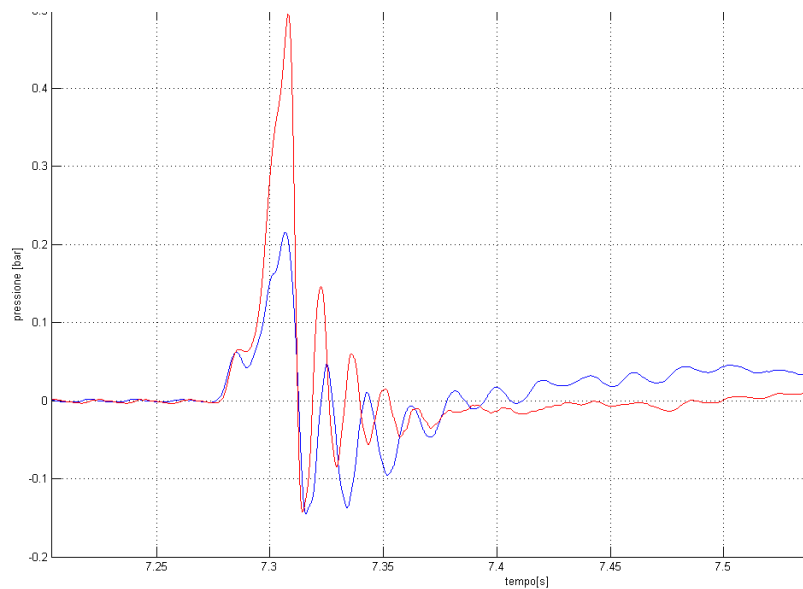
Figure 94 –Pressure plot for the first centesimal of second

3.3.4.6 Comparison for all tests with Explosafe

In Figure 95 all the pressure measurements with Explosafe are reported in pressure and time scale, in order to operate a comparison among all the tests. In fact, in the previous paragraphs, the comparative analysis was essentially operated by considering the homologue water case to the tests done with Explosafe.
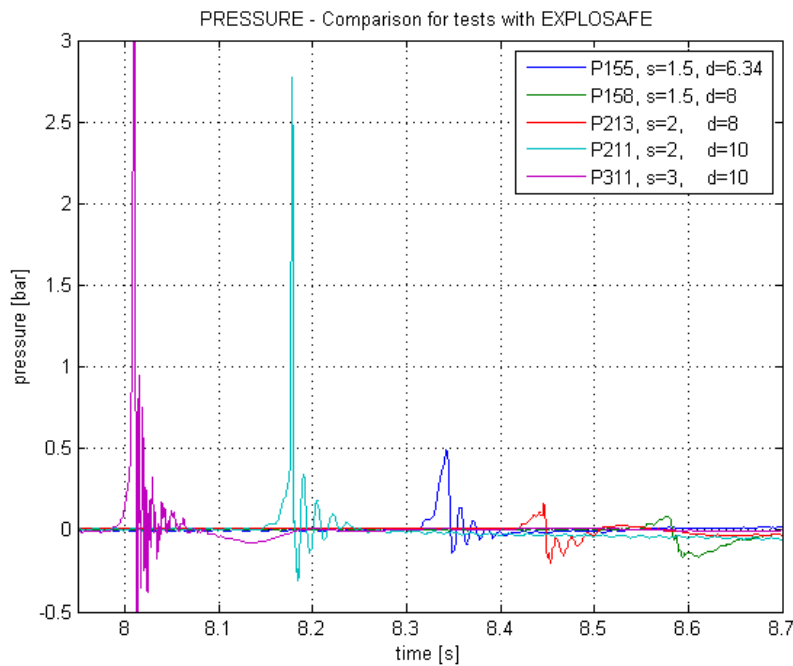
Figure 95 – Pressure wave comparison for tests with Explosafe

The first observation is that sloshing reduction is always present, and in less than one tenth of second all the pressure components are almost equal to the rest value and stable. The result is a confirmation of the Explosafe sloshing reduction capabilities also in the case of projectile impact.

Operated tests suggested also other two comparative considerations on the peak pressure value: one considering as variable parameter the increasing diameter of the projectile and another considering the variation of panel thickness at fixed diameter of the sphere.

The former analysis showed that the tendency was to have a higher pressure wave, the bigger was the projectile.

The only exception to this tendency is given by test number 155, in which a 6.34 mm projectile generated a pressure wave higher than the two cases with the 8 mm

projectile. However, it was already put in evidence that perhaps the 8mm sphere had a particular interaction with the internal filler's cells dimensions.

In Figure 95, panel 309 pressure plot is not reported in order not to disrupt the graph scale readability. By the way, it is easily comparable by seeing at Figure 78: the intensity of the pressure peak is very high, and is a confirmation of the general trend.

The latter analysis suggested to compare pressure plots for experiments done with equal diameter of the sphere and variable thickness of the panel.

The general trend is a higher peak pressure for a thicker panel. Confirmation is given by comparing curve 311 with 211 and curve 213 with 158.

Unfortunately, no data was available for the water case only (in those section only one thickness panel was used for all the tests with pressure transducers). It is left to further studies the possibility to verify if this law is followed also in the case without Explosafe. A possible interpretation to this evidence could be the fact that the thicker is the panel, the higher is the oscillation (or the rupture shock) that it does once it is broken.

4.   CONCLUSIONS

4.1   Final considerations

The main scope of the present thesis was to verify the healing behavior in the case of a new configuration with water impinging the internal side of a S8940 panel. In the case with no internal filler, the reparation is strongly increased probably due to the sustainment that water gives to the panel itself and a positive cooling effect of water. The characteristic parameter used in order to study the behavior is the ratio between the diameter of the thickness of the panel (d) and the diameter of the sphere (s), as in previous works developed inside Politecnico di Milano. The reparation was instantaneous (in the order of magnitude of milliseconds), and only a few drops did exit from the hole before its complete closure.

However, even in the case in which the panel reparation was not complete, a wide percentage of the impact area was repaired. This fact extends the capabilities of preventing fluid leakage form a hypothetic containment system made of S8940, that represents the more direct application. A similar behaviour is a peculiarity of this kind of polymers, and is not verified in the case of impacts on metallic materials such as aluminium or steel, where an hole due to an impact has the same diameter of the impact cross section area. It is interesting to observe that, in addition to self-healing feature, a weight reduction may be achieved compared to metal tank design even in terms of perforation resistance. In fact, a 3mm-ionomer-panel has a ballistic limit (i.e. the minimum velocity at which a panel is perforated by a projectile) at about 165 m/s. A panel of 2.37 mm of 2024-T3 aluminium [25] and one of 0.4 mm of steel [22] have similar ballistic limit. However, in terms of panel weight, considering its lower density, the Surlyn® 8940 solution is convenient with respect to the aluminium alloy and almost equal to the steel one (Table 21). The drawback of polymeric materials is represented by their poor mechanical properties.

	Surlyn®8940	Aluminium (2024-T3)	Steel
Density [kg/m^3]	950	2800	7800
Young modulus [GPa]	0.35	73	210
Thickness [mm]	3	1.02	0.37
Thickness [mm]	2	0.68	0.24

Table 21 – Panel material comparison at equal weight

On the tests made with Explosafe inside the tank, the positive effect on reparation due to water was no more dominant. The performance decrement is probably due to a higher pressure wave in the region just behind the perforated panel and to the physical interaction between the melted ionomer and the sharp aluminium cells of Explosafe. The s/d performance characteristic lines are even below the consolidated performance of the panel in air.
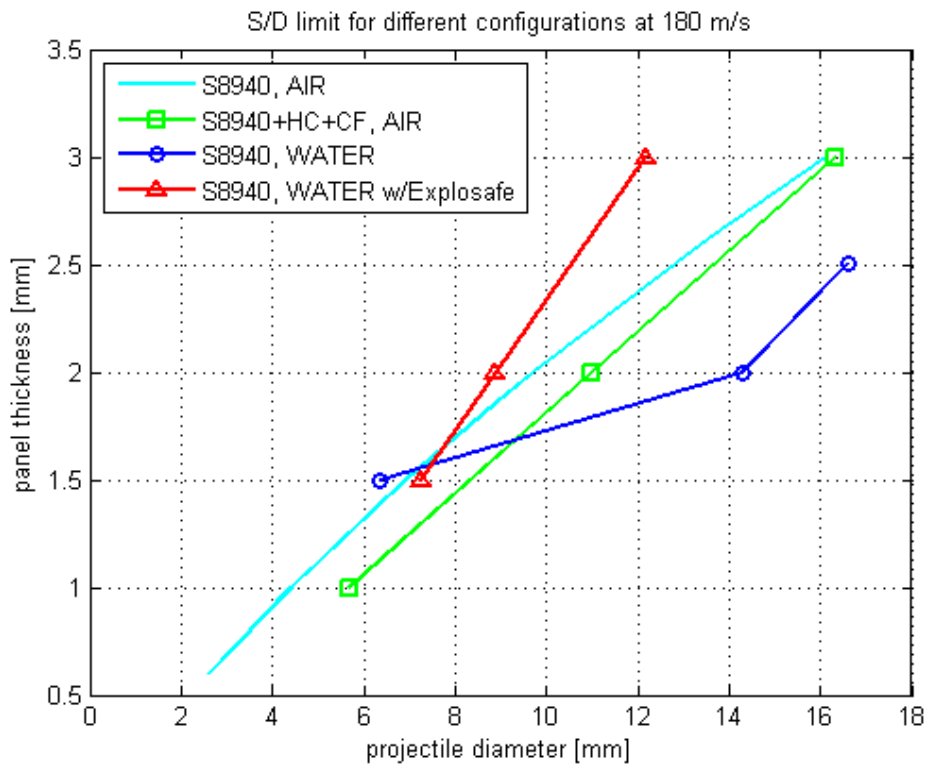
Figure 96 – S/d limit graph for different configurations

Beside this negative feature, experiments with pressure sensors mounted inside the tank showed a reduction in the sloshing wave when Explosafe was present for all the tests. Peak pressure reduction immediately after the ballistic impact was not always experienced, but this fact could be due also to a small tank. Only one experimental campaign had been performed in this past years [15], and for the moment that conclusion is confirmed. This latter part of the test campaign showed also other interesting results: as the projectile diameter increased, the peak pressure was higher, while a thicker panel implied a rise in the peak pressure (the latter consideration has been verified in the case of Explosafe only).
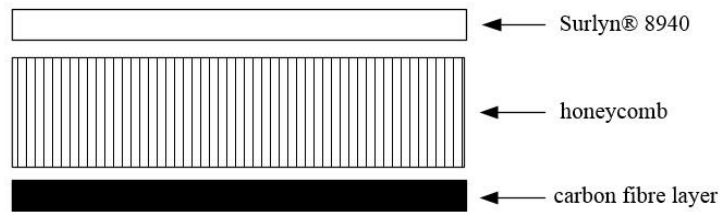
Figure 97 – Multilayer conceptual sketch

s \ d	2.35	3	5	6.34	8	10	12	14.3
1	0.43	0.33	0.20	0.16	0.13	0.10	0.08	0.07
2	0.85	0.67	0.40	0.32	0.25	0.20	0.17	0.14
3	1.28	1.00	0.60	0.47	0.38	0.30	0.25	0.21

Table 22 – s/d limit table for HC in air environment (E. Fedele)

In order to mitigate the performance disruption brought by the insertion of Explosafe, a multilayer proposal (Figure 97) could be considered. In this case, naturally, the performance increase due to water presence is cancelled: however, from Figure 96 it is possible to see that the performance in the case of Explosafe is worse than the case of a multilayer configuration with a Nomex honeycomb and a carbon fibre panel [23]. Tests on this configuration have not been attempted yet in the case of water, and they represent a future possible work. The main concept below this configuration is the capability of unifying the positive healing behaviour of the ionomer and the sloshing reduction of Explosafe with the high mechanical properties of carbon fibre panels.

4.2   Future developments

Future developments can extend in different directions.

A very interesting contribution could be given by the use of a thermal imaging camera to record the temperature of the ionomer during the impact. For the moment, in literature there are three very different values of temperatures for similar impact conditions.

Some tests with a pressurized tank can be helpful to demonstrate the capability of the ionomer for pressurized space applications.

Some numerical model for ballistic limit prediction for metallic materials or common polymers are in development in recent years, and the same modelling could be extended to this class of ionomer.

During the test results' discussion, it was put in evidence that the rupture of the ionomer in case of the Explosafe filled tank could be due to the presence of the aluminium filler itself in the region adjacent to the ionomer. Some tests with the Explosafe positioned at a small distance from the ionomer are advisable, possibly with some more pressure sensors inside the tank to provide a better tracking of the pressure wave.

During the present work, only a cylindrical shaped Explosafe has been used. It should be an opportunity to test also small cylindrical configuration.

References

[1] S. Ghosh, Self-healing materials, Wiley, 2009.

[2] C. De Stasio, «Experimental Characterization of Mechanical Properties and Self-Healing,» Politecnico di Milano, 2014.

[3] F. Herbst, D. Dohler, P. Micael e W. Binder, «Self-healing polymers via supermolecular forces,» *Macromolecular Rapid Comunications,* vol. 3, n. 203-220, 2013.

[4] S. Coppi, «Analisi sperimentale del comportamento di un polimero autoriparante e sviluppo preliminare di un modello viscoelastico,» Politecnico di Milano, 2012.

[5] Walker, Mc Donald, Niki e Aglietti, «Initial assessment of hybrid inflatabel structures,» *Acta Astronautica,* n. 68, pp. 1185-1192, 2011.

[6] V. Vrakking, «Design of a deployable struture for a lunar greeenhouse module,» TU Delft, 2014.

[7] E. Christiansen, «Handbook for designing MMOD protection,» NASA/TM-2009-214785.

[8] R. Burt e E. Christiansen, «Hypervelocity impact testing of transparent spacecraft materials,» *International Journal of Impact Engineering,* n. 29, pp. 153-166, 2003.

[9] S. Ryan e E. Christiansen, «Honeycomb vs. foam: evaluationg potential upgrades to ISS module shielding,» in *International Astronomical Congress (IAC),* 2009.

[10] S. Ryan e E. Christiansen, «Micrometeoroid and orbital debris (MMOD) shiedl ballistic limit analysis program,» NASA/TM-2009-214789.

[11] E. D. W. Layers. [Online]. Available: http://www.esa.int/spaceinimages/Images/2014/06/Hypervelocity_impact_ on_stuffed_Whipple_shield_innermost_layer.

[12] D. Varas, J. Lopez-Puente e R. Zaera, «Experimental analysis of fluid-filled aluminium tubes subjected to high-velocity impact,» *International Journal of Impact Engineering,* n. 36, pp. 81-91, 2009.

[13] A. Szego, K. Premji e R. Appleyard, «Evaluation of Explosafe explosion suppression for aircraft fuel tank protection,» AFWAL-TR-80-2043 (http://www.dtic.mil/dtic/tr/fulltext/u2/a093125.pdf), 1980.

[14] A. Birk, «Review of expanded aluminum products for explosion suppression in containers holding flammable liquids and gases,» *Journal of Loss Prevention in Process Industries,* vol. 21, n. 493-505, 2008.

[15] A. Copland, «Hydrodynamic ram attenuation,» 1983.

[16] R. Fall, «Puncture Reversal of Ethylene Ionomers – Mechanistic Studies,» Virginia Poliytechnic Institute and State University, Master of Science in Chemistry, 2001.

[17] S. Kalista, «Self-Healing of Thermoplastic Poly(Ethylene-co-Methacrylic Acid) Copolymers following projectile punctures,» Virginia Polytechnic Institute and State University, Master of Science in Engineering Mechanics, 2003.

[18] L. Borghetti, G. Janszen e M. Morandini, «Fuel tank explosion protection,» in *International Fire Replacement Working Group*, Bremen, 2000.

[19] «Dupont Surlyn 8940 Properties,» [Online]. Available: http://www.dupont.com/content/dam/dupont/products-and-services/packaging-materials-and-solutions/packaging-materials-and-solutions-landing/documents/surlyn_8940.pdf.

[20] L. Novellino, «Prove di impatti balistici obliqui su materiali autoriparanti,» Politecnico di Milano, Milano, 2014.

[21] [Online]. Available: http://www.ronchetti.it. [Consultato il giorno 01 06 2015].

[22] J. Dean, C. Dunleavy, P. Brownb e T. Clyne, «Energy absorprion during projectile perforation of thin steel plates and the kinetic energy of ejected fragments,» *International Journal of Impact Engineering,* vol. 36, n. 1250-1258, 2009.

[23] E. Fedele, «Comportamento balistico di strutture multistrato sandwich contenenti ionomeri autoriparanti,» Politecnico di Milano, 2013.

[24] Quadrio e S. Zaffaroni, «Caratterizzazione e analisi sperimentale del comportamento balistico di polimeri ionomerici autoriparanti,» Politecnico di Milano, 2012.

[25] M. Loikkanen, M. Buyuk, S. Kan e N. Meng, «A computational and Experimental Analysis of Ballistic Impact to sheet metal aircraft structure,» in *5th European LS-DYNA Users Conference.*

[26] L. Antoinat, R. Kubler, J. Barou, P. Viot e L. Barrallier, «Perforation of aluminium alloy thin plates,» *International Journal of Impact Engineering,* n. 255-267, 2015.

[27] S. Kalista e T. Ward, «Self-healing of poly(ethylene-co-methacrylic acid) copolymers following ballistic puncture,» in *Proceedings of the First International COnference on Self Healing Materials*, Noordwijk aan Zee (The Netherlands), 2007.

[28] S. Van der Zwaag, N. Van Dijk, Jonkers, Mookehoek e Sloof, «Self-healing mehaviour in man-made engineering materials: bioinspired but taking into account their intrinsic character,» *Phil. Trans. R. Soc.,* n. 367, pp. 1689-1704, 2009.

[29] A. Grande, L. Castelnovo, L. Di Landro, C. Giacomuzzo, A. Francesconi e M. Rahman, «Rate-dependent self-healing behaviour of an ethylene-co-methacrylic acid ionomer under high-energy impact conditions,» *Journal of Apllied Polymer Science,* 2013.

[30] S. Kalista e T. Ward, «Thermal characteristics of the self-healing response in poly(ethylene-co-methacrylic acid) copolymers,» *Jorunal of the Royal Society Interface,* n. 4, pp. 405-411, 2007.

[31] S. Ryan, F. Schafer, R. Destefanis e M. Lambert, «A ballistic limit equation for hyperbvelocity impacts on composite honeycomb sandwich panel satellite structures,» *Advances in Space Research,* n. 41, pp. 1152-1166, 2008.

[32] F. Schaefer, S. Ryan, M. Lambert e R. Putzar, «Ballistic limit equation for equipment placed behind satellite structure walls,» *International Journal of Impact Engineering,* n. 35, pp. 1784-1791, 2008.

[33] A. Francesconi, C. Giacomuzzo, A. Grande, T. Mudric, M. Zaccariotto, E. Etemadi, L. Di Landro e U. Galvanetto, «Comparison of self-healing ionomer to aluminium-alloy bumpers for protecting spacecraft equipment from space debris impact,» *Advances in Space Research,* n. 51, pp. 930-940, 2013.

[34] R. Varley e S. Van der Zwaag, «Towards an understanding of thermally activated self-healing of an ionomer system during ballistic penetration,» *Acta Materialia,* n. 56, pp. 5737-5750, 2008.

[35] K. Gordon, P. Penner, P. Bogert, Yost e Siochi, «Puncture Self-healing polymers for Aerospace Applications».

[36] A. Goldsmith, «Ionomer-polymer self-healing material applications,» in *2nd AIAA Unmanned Unlimited Systems Technologies and Operations*, San Diego, California, September 2003.

[37] S. Van der Zwaag, A. Grande, W. Post, S. Garcia e T. Bor, «Review of current strategies to induce self-healing behaviour in fibre reinforced polymer based composites,» *Materials Science and Technology,* vol. 30, n. 13a, pp. 1633-1641, 2014.

[38] M. Kohzaki, Y. Tsujita, A. Takizawa e T. Kinoshita, «The crystallization and formation of cluster of ethylene ionomer during physical aging,» *Journal of Applied Polymer Science,* n. 33, pp. 2393-5402, 1987.

[39] A. Grande, L. Castelnovo, D. L. L., S. G., C. Giacomuzzo e F. A., «Multilayer composites with self-healing capability based on an EMAA ionomer,» in *Proceedings of ICCM19*, Montreal, 2013.

[40] G. Janszen, A. Grande, P. Bettini e L. Di Landro, «Integrated Solutions for safe fuel tanks,» *International Journal of Safety and Security Engineering,* vol. 4, n. 3, pp. 271-279, 2014.

[41] G. Janszen e P. A., «Experimental analysis and numerical simulation of a fuel tank filler in crash environment,» in *Proceedings of 3rd International Conference on Fluid Structure Interaction*, La Coruña, Spain, 2005.

[42] C. Caprile, G. Janszen e M. Morandini, «Study of the effects of a particular fuel tank filler in crash environment,» in *Proceedings of 16th AIDAA National Conference*, Palermo, 2001.

[43] D. Bein, Advanced Technology for Fire Suppression in Aircraft, 2007.

[44] T. Hogan e Pedriani, «Flame Tube and Ballstic Evaluation of Explosafe Aluminium Foil for Aircraft fuel tank explosaion preotection,» USAF AFY1AL-TR-80-2031 (http://oai.dtic.mil/oai/oai?verb=getRecord&metadataPrefix=html&identifier=ADA093542), Ohio, April 1978.

[45] Y. Brodsky, «The European Mars analog station for advanced technology integration (ERAS),» in *IAC-12-E5.2.6.*

[46] Abbud, A. Talib, Mustapha e Ali, «Ballistic limit behaviour of polymer transparent materials under high velocity impact,» *International Journal of Engineering and Technology,* vol. 8, n. 2, pp. 61-66, 2011.

[47] N. Jones e J. Kee Paik, «Impact perforation of aluminium alloy plates,» *International Journal of Impact Engineering,* n. 48, pp. 46-53, 2012.

[48] D. Varas, J. Lopez-Puente e R. Zaera, «Numerical Analysis of the hydrodynamic ram phenomenon in aicraft fuel tanks,» *AIAA Journal,* vol. 50, n. 7, July 2012.

[49] D. Varas, J. Lopez-Puente e R. Zaera, «Numerical modelling of the hydrodynamic ram phenomenon,» *International Journal of Impact Engineering,* n. 36, pp. 363-374, 2009.

[50] K. Shimamura e T. Ootsuka, «Study of water entry of high-speed projectile,» *Procedia Engineering,* n. 58, pp. 232-239, 2013.

[51]   S. Garcia, H. Fischer e S. van der Zwaag, «A critical appraisal of the potential of self healing polymeric coatings,» *Progress in Organic Coatings,* n. 72, pp. 211-221, 2011.